



# Temporal Evolution of the Inverse Evershed Flow

C. Beck<sup>1</sup>  and D. P. Choudhary<sup>2</sup> 

<sup>1</sup>National Solar Observatory (NSO), 3665 Discovery Drive, Boulder, CO 80303, USA; [cbeck@nso.edu](mailto:cbeck@nso.edu)

<sup>2</sup>Department of Physics & Astronomy, California State University, Northridge, CA 91330-8268, USA

Received 2019 November 23; revised 2020 February 10; accepted 2020 February 11; published 2020 March 12

## Abstract

The inverse Evershed flow (IEF) is an inflow of material into the penumbra of sunspots in the solar chromosphere that occurs along dark, elongated super-penumbral fibrils extending from about the outer edge of the moat cell to the sunspot. The IEF channels exhibit brightenings in the penumbra, where the supersonic IEF descends to the photosphere causing shock fronts with localized heating. We used an 1 hr time series of spectroscopic observations of the chromospheric spectral lines of Ca II IR at 854 nm and H $\alpha$  at 656 nm taken with the Interferometric Bidimensional Spectrometer at the Dunn Solar Telescope to investigate the temporal evolution of IEF channels. Complementary information on the photospheric magnetic field was obtained from observations with the Facility Infrared Spectropolarimeter at 1083 nm and the Helioseismic and Magnetic Imager. We find that individual IEF channels are long-lived (10–60 minutes) and only show minor changes in position and flow speed during their lifetime. Initiation and termination of IEF channels takes several minutes. The IEF channels with line-of-sight velocities of about 10 km s<sup>-1</sup> show no lasting impact from transient or oscillatory phenomena with maximal velocity amplitudes of only about 1 km s<sup>-1</sup> that run along them. We could not detect any clear correlation of the location and evolution of IEF channels to local magnetic field properties in the photosphere in the penumbra or moving magnetic features in the sunspot moat. Our results support a picture of the IEF as a field-aligned siphon flow along arched loops. From our data we cannot determine if their evolution is controlled by events at the outer end in the moat or at the inner end in the penumbra.

*Unified Astronomy Thesaurus concepts:* Sunspots (1653); Solar chromosphere (1479); Solar photosphere (1518)

*Supporting material:* animation

## 1. Introduction

The three-dimensional topology of the magnetic field of sunspots supports mass motions and wave propagation along field lines at all heights from the photosphere to the corona (Staude 1999; Solanki 2003; Khomenko & Collados 2015). The dominant mass motions are the Evershed flow (EF; Evershed 1909a) in the photosphere that is directed outward from the sunspot center and the inverse Evershed flow (IEF; Evershed 1909b; Maltby 1975) at chromospheric heights in the opposite direction that sets in at a height of about 500 km (Boerner & Kneer 1992). On rare occasions, photospheric counter-EFs were also observed that were associated with high chromospheric activity (Louis et al. 2014b; Siu-Tapia et al. 2017).

Most wave motions observed in both photospheric and chromospheric lines were found to originate in the umbra or at the umbral boundary and to propagate outwards (Zirin & Stein 1972; Antia et al. 1978; Rouppe van der Voort et al. 2003). Besides these systematic motions, numerous transient phenomena were detected such as chromospheric jets and anomalous flows in sunspots associated with local dynamical magnetic phenomena (Katsukawa et al. 2007; Morton 2012; Louis et al. 2014a). In higher atmospheric layers, coronal rain and flocculent flows were observed which are believed to result from rapid cooling of material at those heights that subsequently slides down along the magnetic field lines (Vissers & Rouppe van der Voort 2012; Ahn et al. 2014).

The photospheric EF is one of the earliest detected phenomena in sunspots and has been studied extensively using both space and ground-based high-resolution instrumentation (Rimmele 1995b; Ichimoto et al. 2007). It starts at so-called

penumbral grains (i.e., bright points at the umbral end of penumbral filaments), flows intermittently radially outward following elevated, nearly horizontal magnetic field lines and ends mostly at the outer penumbral boundary (Johannesson 1993; Beck 2006, 2008; Rimmele & Marino 2006; Franz & Schlichenmaier 2009). The flow velocity decreases systematically with increasing height in the atmosphere already across the line formation region of photospheric lines (Hirzberger & Kneer 2001). The driving mechanism of the EF could be either a siphon flow or magneto-convection (Westendorp Plaza et al. 1997; Schlichenmaier et al. 1998a; Scharmer et al. 2011; Rempel 2012), or a mixture of both. Photospheric counter-Evershed flows (i.e., inward flows in the photospheric penumbra), on the other hand were explained invoking a siphon flow mechanism by Siu-Tapia et al. (2018). The photospheric flows usually stop at about the outer penumbral boundary (Rezaei et al. 2006), but sometimes were seen to extend outward with supersonic velocities (Martínez Pillet et al. 2009). The continuation of the EF beyond the penumbral boundary into the moat region has been studied using both local correlation tracking techniques of magnetic elements and spectropolarimetric observations that showed an association with moving magnetic features (MMFs; Rimmele 1995a; Borrero et al. 2004; Cabrera Solana et al. 2006; Vargas Domínguez et al. 2007).

At chromospheric heights, wave patterns dominate the rapid temporal evolution of the umbra and penumbra. In umbral flashes (Beckers & Tallant 1969; Rouppe van der Voort et al. 2003; Felipe et al. 2010; Houston et al. 2018), large parts of the umbra oscillate coherently leading to shock fronts in the umbral chromosphere. In the penumbra, running penumbral waves (RPWs) are seen, which presumably are magneto-acoustic

waves generated in the photosphere, that propagate radially outwards at chromospheric layers and dissipate energy at chromospheric or coronal heights (Tziotziou et al. 2006; Bloomfield et al. 2007; Jess et al. 2013, 2015; Krishna Prasad et al. 2015; Grant et al. 2018).

Steady and longer-lived mass motions are observed as the IEF at chromospheric heights and above that transport material into the sunspot from the super-penumbral boundary and beyond as first observed by Evershed (1909b) and later extensively studied by St. John (1913). St. John (1913) found IEF velocities of about  $3 \text{ km s}^{-1}$ , which were much higher than EF velocities seen at that time, a fact that was confirmed by Bones & Maltby (1978). Spectroscopic measurements based on  $\text{H}\alpha$  spectra showed higher IEF velocities of up to  $50 \text{ km s}^{-1}$  (Beckers 1962; Haugen 1969; Maltby 1975; Alissandrakis et al. 1988; Dere et al. 1990; Choudhary & Beck 2018), which exceed the chromospheric sound speed. The transition region IEF velocities were found to be of the order of a few  $10 \text{ km s}^{-1}$  (Alissandrakis et al. 1988; Dere et al. 1990; Kjeldseth-Moe et al. 1993; Teriaca et al. 2008). A siphon flow is thought to be the most likely mechanism among the several theoretical ideas that were considered to drive the IEF such as gravitationally driven downflows or moving flux tubes (Beckers 1962; Montesinos & Thomas 1997; Teriaca et al. 2008).

The properties of the flow channels carrying the IEF were derived in recent years through various techniques using modern spectropolarimetry and adaptive optics. From  $\text{H}\alpha$  filtergrams it was found earlier that the IEF channels contain compression shocks, last for about 70 minutes to more than 2 hours, and that in many cases old channels are replaced by new ones (Maltby 1975, 1997). The flow channels are inclined to the local vertical in the range of  $30^\circ$ – $80^\circ$  (Haugen 1969; Beck & Choudhary 2019). Comprehensive studies of the temporal evolution of both EF and IEF have been carried out using observations with the universal Birefringent Filter at the Dunn Solar Telescope (DST) in the photospheric Fe I line at  $557.6 \text{ nm}$  and the chromospheric  $\text{H}\alpha$  line (Georgakilas & Christopoulou 2003). Their results show a complex pattern of mass motions and waves at both photospheric and chromospheric heights with the EF, IEF, RPWs, and an additional outward radial motion of “velocity packets” at a speed of  $5$ – $6 \text{ km s}^{-1}$ . These “velocity packets” were defined by Georgakilas & Christopoulou (2003) as small patches of velocities with an opposite sign to the IEF of a few Mm extent in the outer penumbra and the moat region. A generic problem of some older studies on the IEF is that because of the spatial and temporal resolution of the data available at the time these different phenomena can get mixed up.

In this paper, we study the temporal evolution of the IEF using high-resolution spectroscopic and spectropolarimetric observations in multiple spectral lines that originate at different atmospheric heights. Our data analysis clearly shows both the IEF and wave phenomena such as RPWs and their interaction in different diagnostics. However, here we shall focus only on the temporal character of the IEF and postpone the study of the interaction with different types of waves. The semi-stationary IEF is only impacted in a minor way by the transient waves and in general shows velocities that are an order of magnitude larger than the wave amplitudes.

To avoid a confusion of different phenomena, we define for the current study the chromospheric IEF channels as super-penumbral, radially oriented fibrils that connect the penumbra

with the super-penumbral boundary and that exhibit a significant flow velocity (e.g., Figures 1 and 2 and the animation). As in our previous paper, we define the downflow points of IEF channels as the locations close to the penumbral boundary with about maximal velocity and an enhanced brightness due to shock fronts (Choudhary & Beck 2018, in the following Paper I). The RPWs are the concentric dark and bright circles or circle arcs in the intensity and velocity images with the sunspot as the center and show up as inclined ridges in the penumbra in spacetime plots. We differentiate in addition between IEF channels and super-penumbral filaments by the latter permanently exhibiting a strongly reduced intensity and flows along a large part of their length. There are only a few such filaments in the field of view (FOV) going to the left and down during the period of our observations (Figures 1 and 2). The definition of the “velocity packets” follows that of Georgakilas & Christopoulou (2003), given above.

Section 2 describes our data sets whose analysis is detailed in Section 3. Our results are presented and summarized in Sections 4 and 5, respectively. Section 6 discusses our findings, while Section 7 presents our conclusions.

## 2. Observations

We observed the decaying active region (AR) NOAA 12418 on 2015 September 16 with the Interferometric Bidimensional Spectrometer (IBIS; Cavallini 2006; Reardon & Cavallini 2008) and the Facility Infrared Spectropolarimeter (FIRS; Jaeggli et al. 2010) at the DST (Dunn 1969; Dunn & Smartt 1991). The FOV covered the isolated leading sunspot of the AR located at about  $x, y = -500'', -340''$  at a heliocentric angle of about  $43^\circ$ . The trailing opposite polarity toward the east had already decayed to diffuse plage and network.

IBIS sequentially scanned the two chromospheric spectral lines of  $\text{H}\alpha$  at  $656 \text{ nm}$  and  $\text{Ca II IR}$  at  $854.2 \text{ nm}$  in its spectroscopic mode with a non-equidistant spectral sampling of 27 and 30 wavelength points, respectively. The exposure time was 40 ms with a total cadence for one spectral scan of 11.2 s. From UT 14:42 until 15:56, 400 spectral scans were acquired. The 11 spectral scans Nos. 180 to 190 from UT 15:16 to 15:17 were impacted by clouds and were all replaced with the scan No. 179. The IBIS FOV spanned a circular aperture with a diameter of  $95''$  at a spatial sampling of  $0''.095 \text{ pixel}^{-1}$ .

With FIRS we recorded vector spectropolarimetric data in a wavelength range from  $1081.37$  to  $1085.28 \text{ nm}$  with a dispersion of  $3.84 \text{ pm pixel}^{-1}$  that covered the photospheric Zeeman-sensitive Si I line at  $1082.7 \text{ nm}$  and the chromospheric He I line at  $1083 \text{ nm}$ . We obtained one large-scale spatial map of 250 steps with a step width of  $0''.3$  from UT 14:42 until 14:55. The spatial sampling along the  $72''$  long slit of  $0''.3$  width was  $0''.15 \text{ pixel}^{-1}$ . The total integration time per step was only 2 s to focus on the thermodynamics of the He I line instead of its polarization signal or any derived chromospheric magnetic field.

The ground-based data are complemented with the Milne–Eddington inversion results for the photospheric magnetic field (inclination  $\gamma$ , field strength  $B$ , line-of-sight (LOS) magnetic flux  $\Phi$ ) derived from observations by the Helioseismic and Magnetic Imager (HMI; Scherrer et al. 2012) on board the *Solar Dynamics Observatory* (SDO; Pesnell et al. 2012). These HMI data cover the whole solar disk with a spatial sampling of about  $0''.5$  at a cadence of 12 minutes.

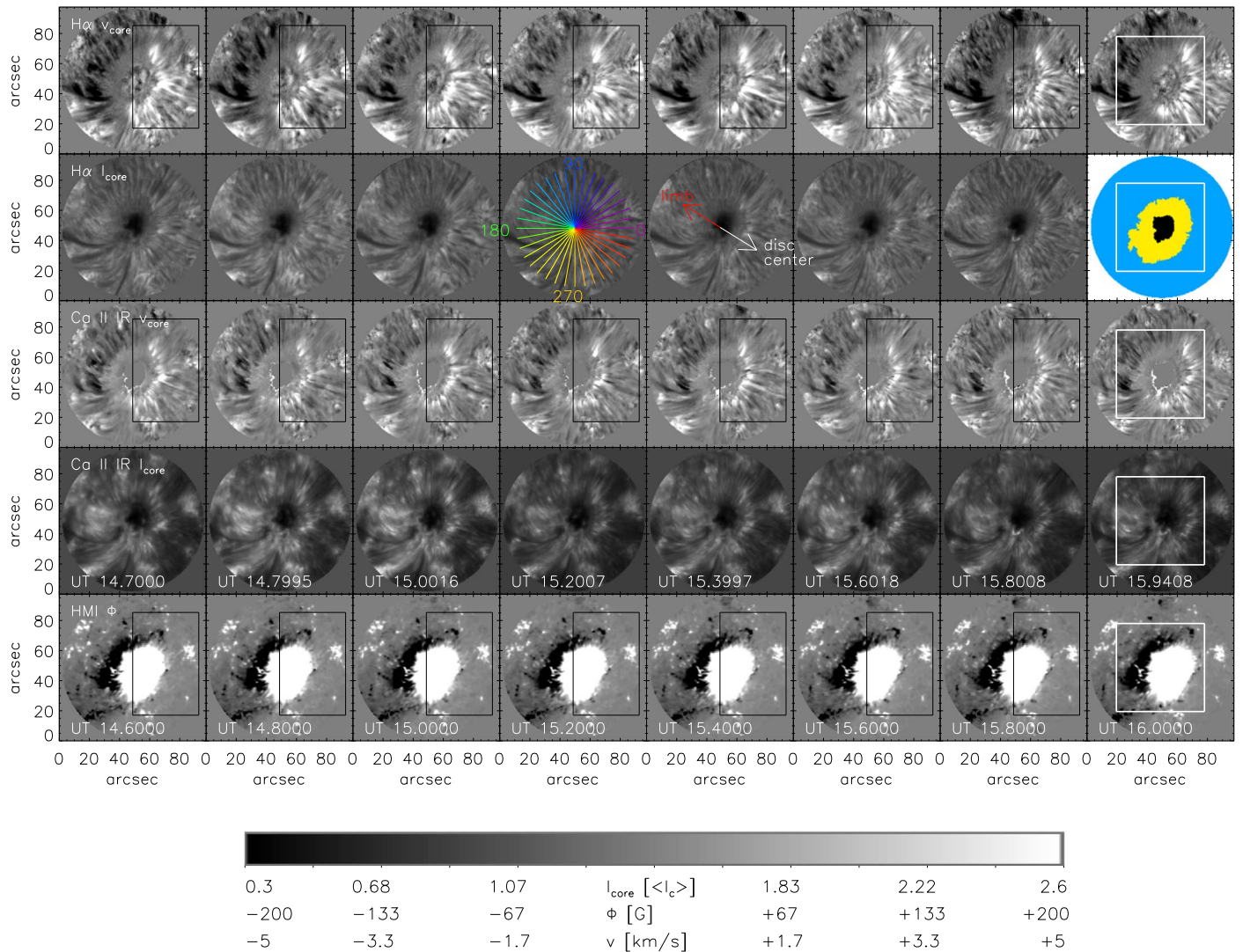


**Figure 1.** Aligned HMI and IBIS data. Bottom to top: HMI LOS magnetic flux  $\Phi$  in the range of  $\pm 200$  G, IBIS line-core intensity and line-core velocity ( $\pm 5$  km s $^{-1}$ ) of Ca II IR, IBIS line-core intensity and line-core velocity ( $\pm 5$  km s $^{-1}$ ) of H $\alpha$ . Time increases from left to right as indicated in the bottom two rows. The black rectangles mark the center side region with the clearest IEF channels. The white squares in the last column indicate the averaging region used for the correction of the prefilter transmission in the IBIS spectra. The colored mask in the fourth row of the last column shows the umbral and penumbral boundaries used for defining the velocity zero-point in H $\alpha$  (black region) and Ca II IR (blue region), respectively. The colored lines in the 4th row and column show the location of the radial cuts around the sunspot center with a  $10^\circ$  spacing, where  $0^\circ$  corresponds to right and  $90^\circ$  to up. The symmetry line of the sunspot is tilted by  $32^\circ$  to the right. An animation of the time series is available in the online material. In addition to the line-core intensity and velocity maps of the two spectral lines corresponding to the top four rows in the figure, it shows azimuthal plots (see the top panel of Figure 4 below) of the Ca II IR line-core intensity (third column at bottom in the animation), the H $\alpha$  line-core velocity (third column at top), the azimuthal derivative  $\frac{dv}{d\phi}$  (fourth column at bottom) and the temporal derivative  $\frac{dv}{dt}$  (fourth column at top) of the H $\alpha$  line-core velocity in the azimuthal display. The latter two panels reveal the short-lived periodic sunspot oscillations in contrast to the long-lived IEF channels. The video begins at 14:41:59 UT and ends at 15:56:26 UT. The real-time video duration is 16 s.

(An animation of this figure is available.)

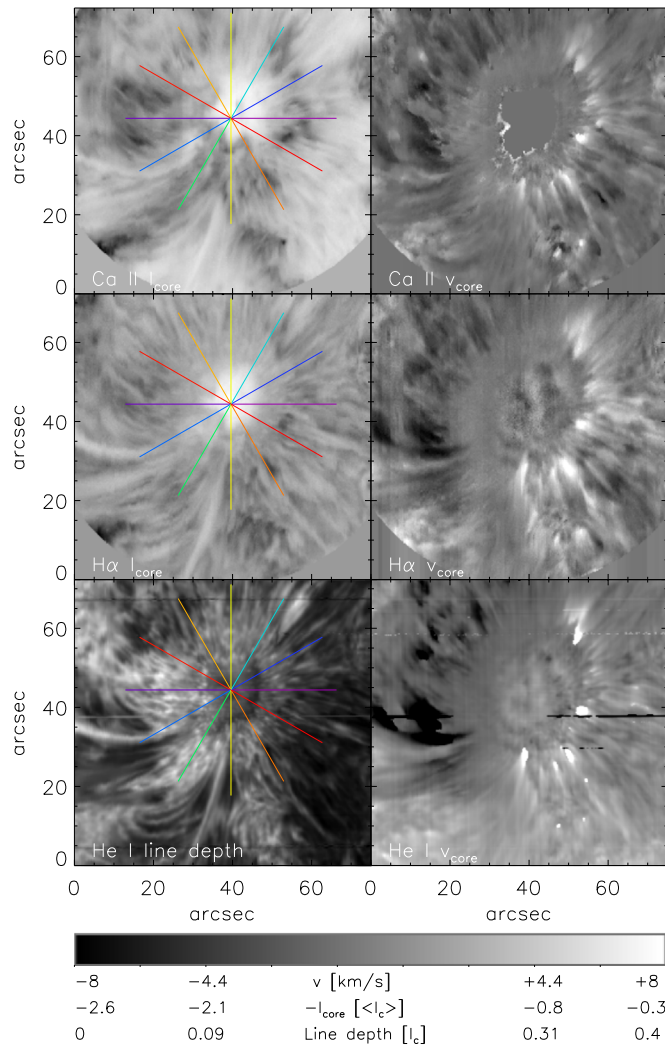
All IBIS spectral scans were aligned to each other through a correlation of subsequent images of the continuum intensity  $I_c$  in each spectral line and a subsequent shift in  $x$  and  $y$  with  $I_c$  of H $\alpha$  as reference. The same approach was used to align the HMI data. The FOV of the ground-based data was already almost stationary because of the real-time correction by the adaptive optics system of the DST (Rimmele 2004).

Figure 1 shows aligned IBIS and HMI data at the 12 minutes cadence of the latter.

### 3. Data Analysis

#### 3.1. FIRS Data at 1083 nm

We inverted the polarimetric spectra of the Si I line at 1082.7 nm with the Stokes Inversion based on Response functions code (SIR; Ruiz Cobo & del Toro Iniesta 1992). We used a single magnetic component with the magnetic field properties field strength  $B$ , inclination  $\gamma$ , and azimuth  $\phi$  constant with optical depth for all pixels with a significant polarization signal above about 1% of  $I_c$ . The LOS velocity was fitted using gradients with optical depth. Temperature was allowed to vary on two nodes and an additional contribution of unpolarized stray light was used. The stray-light contribution is



**Figure 2.** FIRS data and IBIS pseudo-scan maps. Left column, bottom to top: relative line depth of He I 1083 nm, line-core intensity of H $\alpha$  and Ca II IR in reverse gray scale. Right column, bottom to top: LOS velocity of He I, H $\alpha$  and Ca II IR. The colored lines in the left column indicate the radial cuts with 30° spacing.

a free fit parameter and varied across the FOV from up to 90% in the quiet Sun to less than 1% in the penumbra and umbra in some cases. In the SIR code, the stray light is handled as a fractional contribution of an average profile, usually calculated in a quiet Sun region (see, e.g., Beck & Rezaei 2009, their Equation (1)). Its value in the one-component inversion setup used here represents a mixture of local stray light from the spatial point-spread function (PSF), global stray light from the far wings of the PSF (Beck et al. 2011) and the magnetic fill factor inside the pixel in the case of unresolved magnetic fields in the quiet Sun (Beck & Rezaei 2009). For all pixels without significant polarization signal, a single non-magnetic component was used instead. The SIR code uses the assumption of local thermodynamic equilibrium (LTE). Non-LTE effects near the line core in the intensity spectrum of the Si I line at 1082.7 nm are discussed in Bard & Carlsson (2008) and Shchukina et al. (2017), but Kuckein et al. (2012) and Joshi et al. (2016) found a negligible impact on the inferred magnetic field and LOS velocities. The NLTE effects affect primarily the temperature stratification obtained.

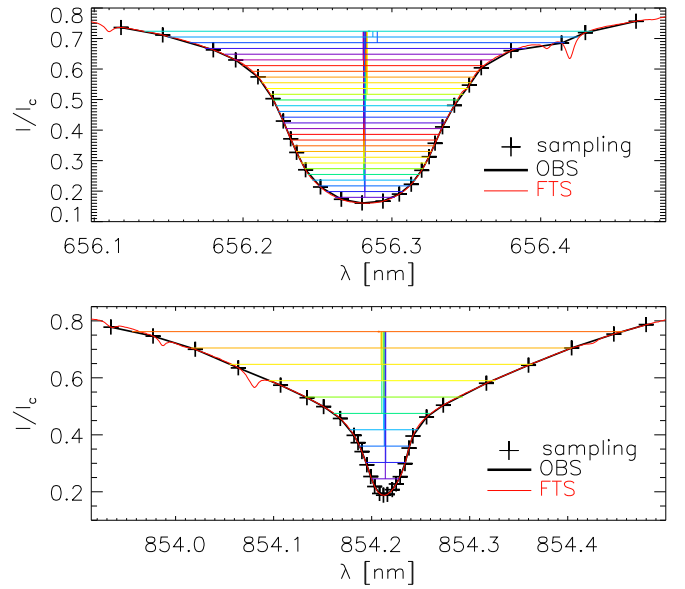


**Figure 3.** Example of the bisector analysis for H $\alpha$  (top panel) and Ca II IR (bottom panel) for the average profile of one scan. The horizontal colored lines indicate the bisectors that are defined by bisector intensity value, central position and width.

For the direct comparison of the FIRS and IBIS data, we created a pseudo-scan map from the IBIS time series (e.g., Beck et al. 2007, Appendix B.2). A simulated slit with a width of 0'3 and a length of 72" was stepped across the IBIS FOV in steps of 0'3. At each scan step of FIRS, the data below the location of the simulated slit at that moment was cut out from the IBIS spectral scan closest in time to the FIRS scan step. The creation of the pseudo-scan map then only depends on providing the initial position of the simulated slit inside the IBIS FOV in  $x$  and  $y$  at the first step. Figure 2 shows the resulting spatially and temporally aligned FIRS and IBIS pseudo-scan maps for the line-core intensities and line-core velocities of He I at 1083 nm, H $\alpha$  and Ca II IR.

### 3.2. IBIS H $\alpha$ and Ca II IR Spectra

We ran a bisector analysis over all H $\alpha$  and Ca II IR spectra from IBIS. The bisector analysis (see Figure 3) determined the bisector velocity (central position), bisector intensity (intensity value), and bisector width (length of the bisector) for 30 (10) bisector levels in steps of 3 (10)% of the relative line depth  $LD = (I_c - I_{\text{core}}) / I_c$  for H $\alpha$  (Ca II IR). The observed spectrum of each spectral scan averaged over the area of the white squares in the last column of Figure 1 was first matched to the reference spectrum from the Fourier Transform Spectrometer atlas (Kurucz et al. 1984) with a correction for the transmission of the IBIS prefilter as described for instance in Beck et al. (2019). The spectra were also re-sampled to a denser wavelength grid prior to the bisector analysis. As the range of the spectral scanning did not reach continuum levels, the first wavelength point of each spectral line (656.12 and 853.93 nm; see Figure 3) was substituted for  $I_c$ . The line depth and the corresponding relative intensity values at fractional line depth were calculated separately for each and every spectrum (i.e.,  $LD = LD(x, y)$ ) and thus vary across the FOV and with time. We used the bisector velocities at 85 (70)% line depth for H $\alpha$  (Ca II IR) in the following as “line-core” velocities. They are more reliable and robust than levels closer to the line core

because of the flatness of the profile of  $H\alpha$  around the line core and the occurrence of emission peaks in Ca II IR, especially in the umbra. We still have set the umbral velocities of Ca II IR to zero in some plots, as they are often spurious even at 70% line depth. In each spectral scan, the average umbral line-core velocity (black region in the fourth row of the rightmost column of Figure 1) was set to zero for  $H\alpha$ , while for Ca II IR the average velocity outside the sunspot (blue region) was used as the reference velocity.

The left four panels of the animation `anim_combined_small.mp4` show the line-core intensity and velocity of  $H\alpha$  and Ca II IR over all 400 spectral scans, while the rightmost column shows the temporal and azimuthal derivative of the  $H\alpha$  velocity. In addition to the IEF channels in and near the penumbra, various other features such as umbral oscillations, RPWs, large-scale filaments, and a potential reconnection event can be seen.

### 3.3. Extraction of Radial Cuts

For the analysis of the results, we extracted all relevant quantities such as spectral line parameters, bisector values, and inversion results on radial cuts. These cuts were set to start at the center of the sunspot and then sample the azimuthal variation on an angular step width of  $1^\circ$ . The zero-point for the angle is to the right, and the angle increases counterclockwise. The symmetry line of the sunspot with about zero LOS velocities (i.e., the direction perpendicular to the connection between sunspot and disk center) goes from about  $60^\circ$  to  $240^\circ$  in azimuth. Each cut extended over a length of  $38''$  on 600 points with a spatial radial sampling of  $\approx 0''.06$  per point. A subset of the cuts is indicated in the middle panel of Figure 1 and the left column of Figure 2. The same cuts were extracted from all spectral scans of IBIS, the FIRS data, and the IBIS pseudo-scan maps.

We determined the radial distance of the umbral and penumbral boundary for each azimuth angle by thresholds in the continuum intensity (blue and red lines in the top panel of Figure 4). The average umbral and penumbral radius were  $8''$  and  $19''$ , respectively. For the automatic detection of the location of IEF channels in all spectral scans we also defined a minimal and maximal radial distance inside which the majority of the IEF channels are visible (black lines in top panel of Figure 4 and black lines in Figure 12 below). Local LOS velocity extrema outside of these boundaries were not counted and are considered to correspond to events other than IEF channels. The IEF channels on the limb side are seen further away from the sunspot center because of the projection effects.

## 4. Results

### 4.1. Temporal Evolution of IEF Channels

#### 4.1.1. Lifetime

To estimate the lifetime of individual IEF channels, we used the temporal evolution for each azimuth angle as shown in the lower panel of Figure 4 for an azimuth of  $0^\circ$ . We determined the maximum value of the unsigned LOS velocity within the radial range for each azimuth angle given by the black lines in the upper panel of Figure 4.

The bottom-left panel of Figure 5 shows these maximal LOS velocities as a function of the azimuth angle and time. Continuous vertical white streaks of increased velocities

indicate the extended presence of an IEF channel. Their length varies from about 10 to over 60 minutes. Some IEF channels exist at about the same place for the whole duration of the time series. The majority of the channels seems to exist for significantly more than 10 minutes. There are several occasions where an existing IEF channel is replaced by a new one rather than completely disappearing, which can be better seen in the animation `anim_combined_small.mp4`. The IEF channels show only little radial motion during their existence (top-left panel of Figure 5).

To better quantify the lifetimes of individual IEF channels, we first applied a slight smoothing to the azimuth-time velocity image of Figure 5 to eliminate some small-scale spurious velocity values. As many of the IEF channels are so close to each other in azimuth that their velocity signatures overlap, we manually added separation lines between the most clearly defined IEF channels (vertical black lines in the right column of Figure 5). Running a contour plot with a velocity threshold of  $1.25 \text{ km s}^{-1}$  over the image then provided a binary mask of all temporally and/or azimuthally continuous velocity patches with a speed above the threshold (top-right panel of Figure 5) that should correspond to individual IEF channels. The lifetime can then be derived from the first to last point of time that each patch is present. Figure 6 shows the histogram of the resulting lifetimes of the about 60 IEF channels in the binary mask. The lifetime shows a flat distribution ranging again from about 10 to 60 minutes.

Figure 7 shows the temporal evolution of the maximal unsigned velocity within the radial boundaries given by the black lines in Figure 4 at nine azimuth angles as another independent determination of the lifetime. The LOS velocities of  $H\alpha$  and Ca II IR closely match each other. Again, increased velocities indicating an IEF channel persist over usually at least 10 minutes with some continuing over up to 60 minutes. We note that lateral motions of the IEF channels can lead to the disappearance of the velocity signature at a fixed azimuth angle in that case.

As final estimate of the lifetime of IEF channels we calculated the temporal auto-correlation of velocities across the time series. We restricted the range in azimuth to  $0^\circ$ – $90^\circ$  and  $270^\circ$ – $360^\circ$  for this calculation to avoid the presence of the long-lived filament structure on the limb side at an azimuth of about  $200^\circ$ . We calculated the auto-correlation for three radial ranges covering the umbra, the locations of the IEF channels, and the sunspot moat beyond the upper radial boundary of the IEF locations. The temporal auto-correlation for the umbra shows a clear oscillatory pattern opposite to the IEF channels and the moat (left column of Figure 8). We thus averaged the auto-correlation over about one period of the umbral oscillations for a clearer picture (right column of Figure 8). In that form, it is obvious that the umbral auto-correlation drops fastest to about zero over less than 300 s. The auto-correlation for the moat region decays slower and closely follows a purely exponential decay with a decay constant of 300 s (e.g., the orange dotted line in the lower panel of Figure 8). The temporal auto-correlation for the region of the IEF channels decays faster than that of the moat region below 200 s, but maintains an extended tail of higher correlation values from about 500 to 1800 s, indicating again the persistence of some structures in the IEF channel region over timescales of 10 minutes or more. Maltby (1975) determined a similar quantity as the auto-correlation that he defined as the number of IEF channels with

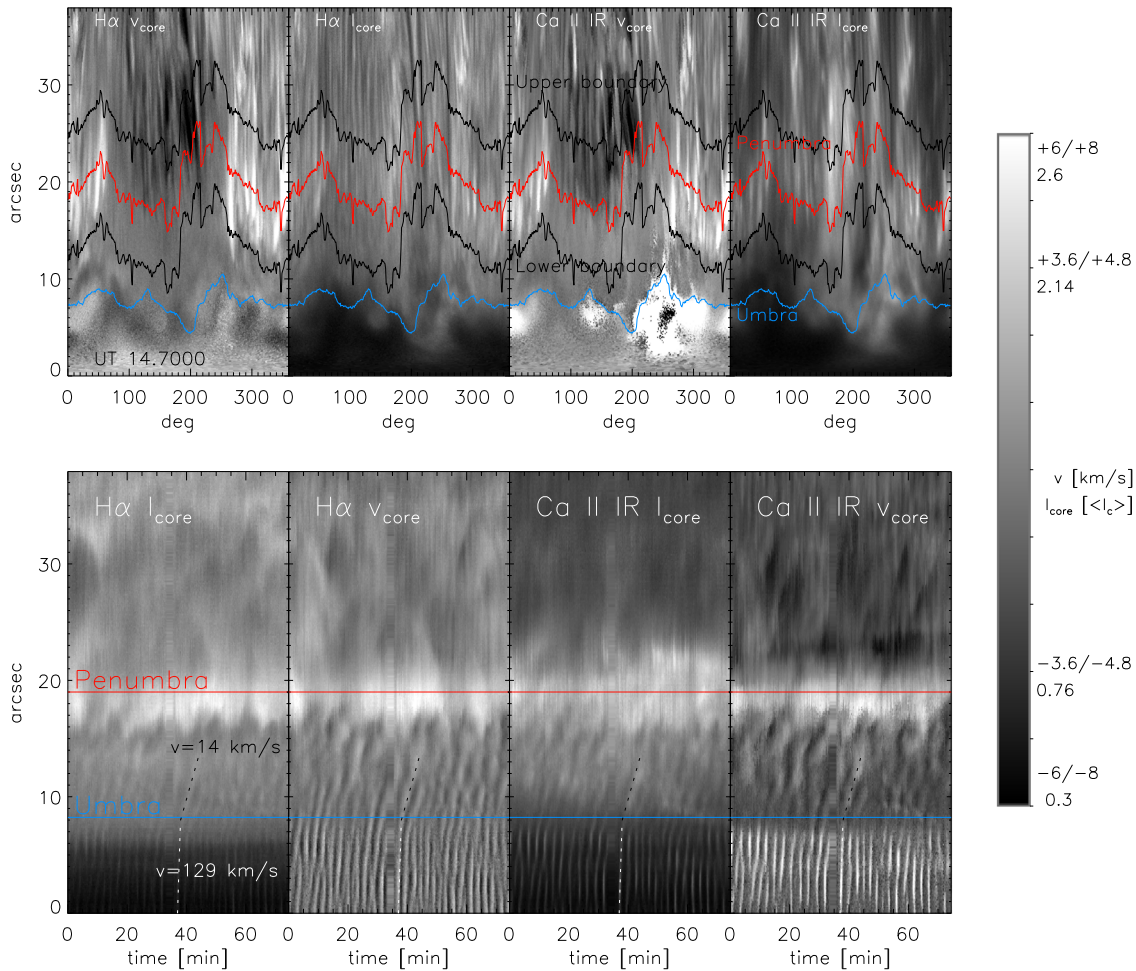


**Figure 4.** Line parameters along radial cuts. Bottom panel: temporal evolution at azimuth  $0^\circ$  for (left to right) line-core intensity and velocity ( $\pm 8 \text{ km s}^{-1}$ ) of  $\text{H}\alpha$ , and line-core intensity and velocity ( $\pm 8 \text{ km s}^{-1}$ ) of  $\text{Ca II IR}$ . The blue and red horizontal lines indicate the average radial distance of the outer umbral and penumbral boundary. The inclined dashed black (white) line indicates an apparent radial propagation speed of  $14 \text{ km s}^{-1}$  ( $129 \text{ km s}^{-1}$ ) in the penumbra (umbra). Top panel: azimuthal variation of the same quantities for the first spectral scan with a  $\pm 6 \text{ km s}^{-1}$  range for the velocities. The blue and red lines indicate the umbral and penumbral boundary. The black lines indicate the radial range that encloses most IEF channels.

unchanged velocity after a given time delay. We read off the corresponding values from his Figure 7, scaled them to be about unity at zero time delay, and over-plotted his results on the auto-correlation. The slope of his curve for  $t < 400 \text{ s}$  matches well with our result. Equalizing the values for long time delays  $t > 1500 \text{ s}$  would make the match of the curves even closer.

#### 4.1.2. Start and End of IEF Channels

With the constant evolution of the velocity pattern including the merging and splitting of IEF channels, it is rather difficult to unambiguously identify the start or end of a specific IEF channel. We manually identified four cases of the termination of halfway isolated IEF channels that did not get replaced instantly and two cases of the start of a flow.

Figure 9 shows the temporal evolution of one event of the start of an IEF channel that began at about UT 15:21 at an azimuth angle of  $327^\circ$ . The LOS velocity is not zero in the beginning from a previous IEF channel. The flow speed at the location marked with the vertical lines approximately doubles from about  $6$  to  $12 \text{ km s}^{-1}$  and the increased velocity then persists for several minutes. There is almost no radial motion of the location of maximal velocity, with potentially a really small

displacement toward the umbra. Figure 10 shows the opposite case of a termination of an IEF channel at about UT 14:44 at an azimuth angle of  $351^\circ$ . The flow speed reduces from about  $12$  to  $0 \text{ km s}^{-1}$  in  $\text{Ca II IR}$ , while in  $\text{H}\alpha$  a residual peak with a speed of about  $3 \text{ km s}^{-1}$  remains that moves away from the umbra by a few arcseconds along with the decrease of the flow speed.

Figure 11 and Table 1 summarize the temporal evolution of the six cases of start and end of an IEF channel that we manually identified. The deceleration at the end seems to be about twice as fast as the acceleration at the start of an IEF channel. The corresponding velocity would change from about sound speed to zero in less than 3 minutes (bottom row of Table 1), while in the opposite direction it takes about 8–10 minutes to reach sound speed when starting from zero. The deceleration derived from the change in the LOS velocity at a fixed spatial location (Figure 11) is likely to be somewhat overestimated because of the additional outwards radial motion of the IEF downflow point, but in general the deceleration of an IEF channels seems to be faster than its acceleration. The acceleration falls short of the one corresponding to free fall by an order of magnitude. For comparison, we derived the corresponding acceleration for the steady-state solution of a critical siphon flow of Montesinos & Thomas (1993) from the

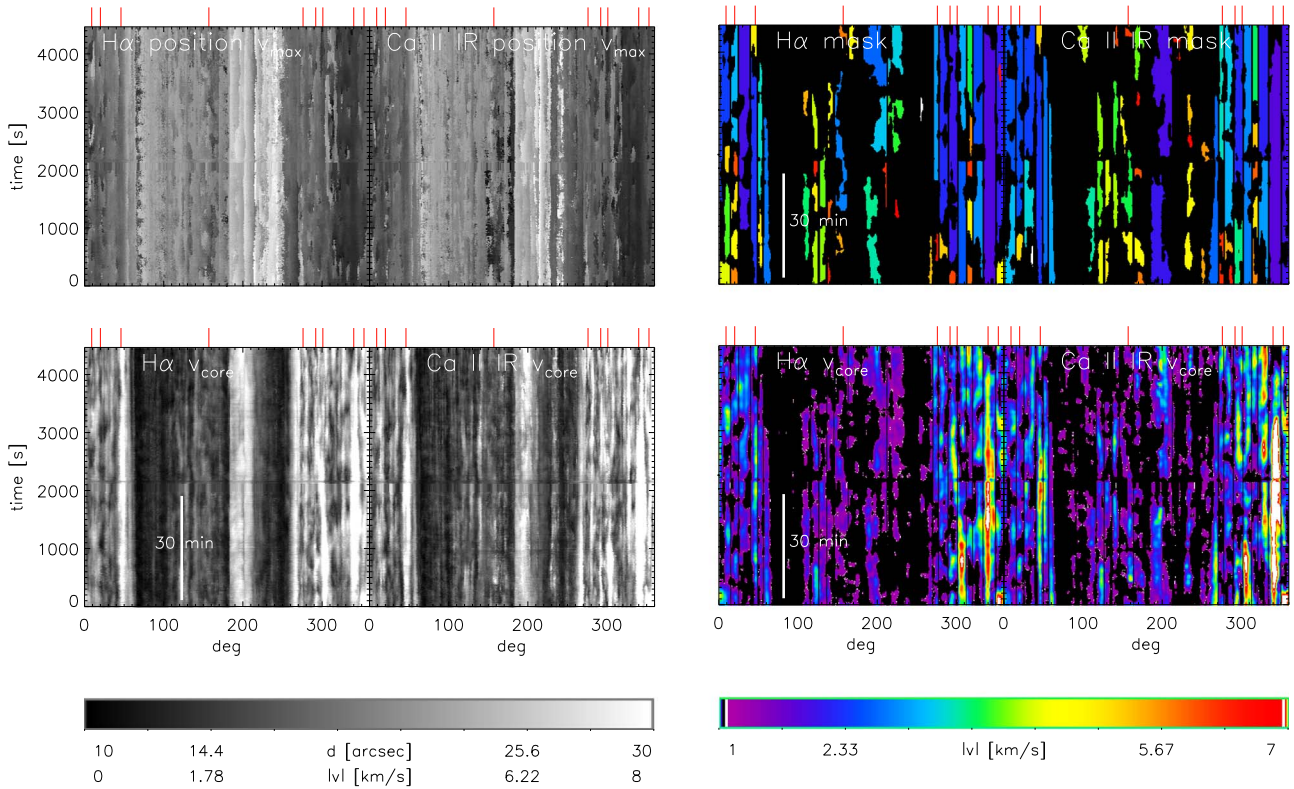


**Figure 5.** Temporal evolution of the unsigned maximal LOS velocities as a function of azimuth and derivation of lifetime. Bottom-left panel: absolute maximal LOS velocities of H $\alpha$  and Ca II IR from 0 to 8 km s<sup>-1</sup>. The maximal velocities were determined between the black lines indicated in the upper panel of Figure 4 for each azimuth angle in each spectral scan. The vertical white bar indicates a duration of 30 minutes. The short red bars at the top indicate the azimuth angles displayed in Figure 7. Top-left panel: radial distance of the velocity maximum in arcsec from the sunspot center. Bottom-right panel: velocities after slight spatial smoothing with a lower threshold of 1 km s<sup>-1</sup> and manually inserted, vertical separation lines between adjacent IEF channels. Top-right panel: mask of individual IEF channels identified.

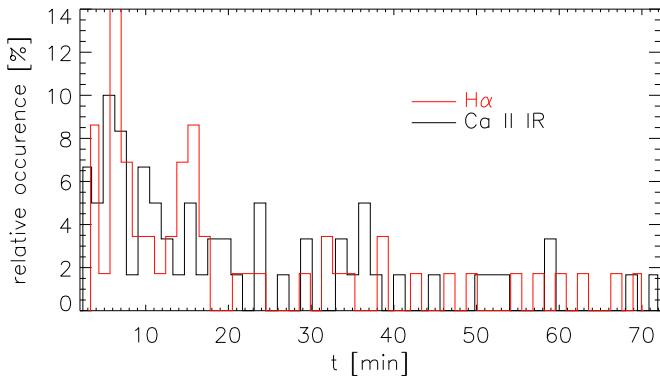


**Figure 6.** Histogram of the lifetime of IEF channels. Black (red) line: derived from the velocity of Ca II IR (H $\alpha$ ).

middle panel of their Figure 3. The flow in their case accelerates from about 3 to 6 km s<sup>-1</sup> over a distance of 300 km with a linear velocity increase. Using the average velocity of 4.5 km s<sup>-1</sup> for covering the distance yields an acceleration of about 45 m s<sup>-2</sup>, which matches our deceleration values.

4.2. Locations of IEF Channels

In Paper I and Beck & Choudhary (2019) we were only able to track 100 manually identified IEF channels in observations at a low cadence of about 20 minutes. The current IBIS time series allows us to increase the statistics on the locations of IEF channels and downflow points to more than 10,000. Given the

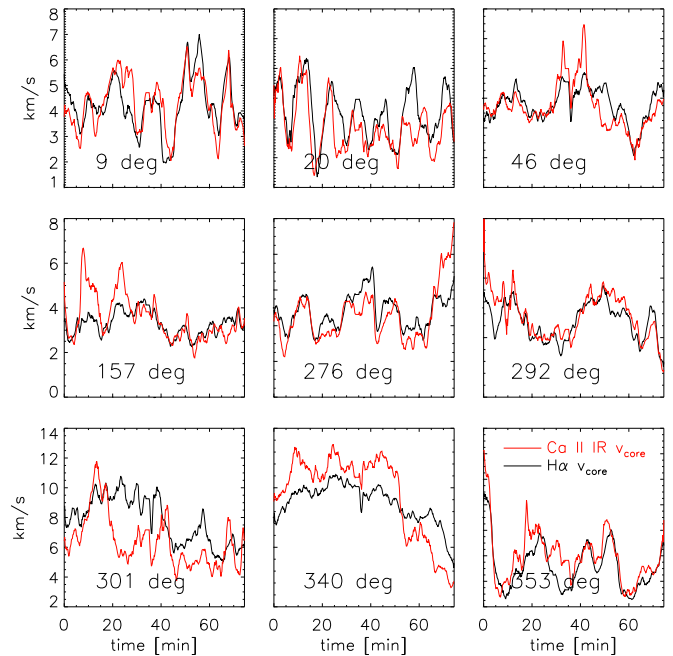


**Figure 7.** Temporal evolution of the absolute velocity for nine azimuth angles. Black/red lines: LOS velocity of H $\alpha$ /Ca II IR. The azimuth angle is indicated in each panel.

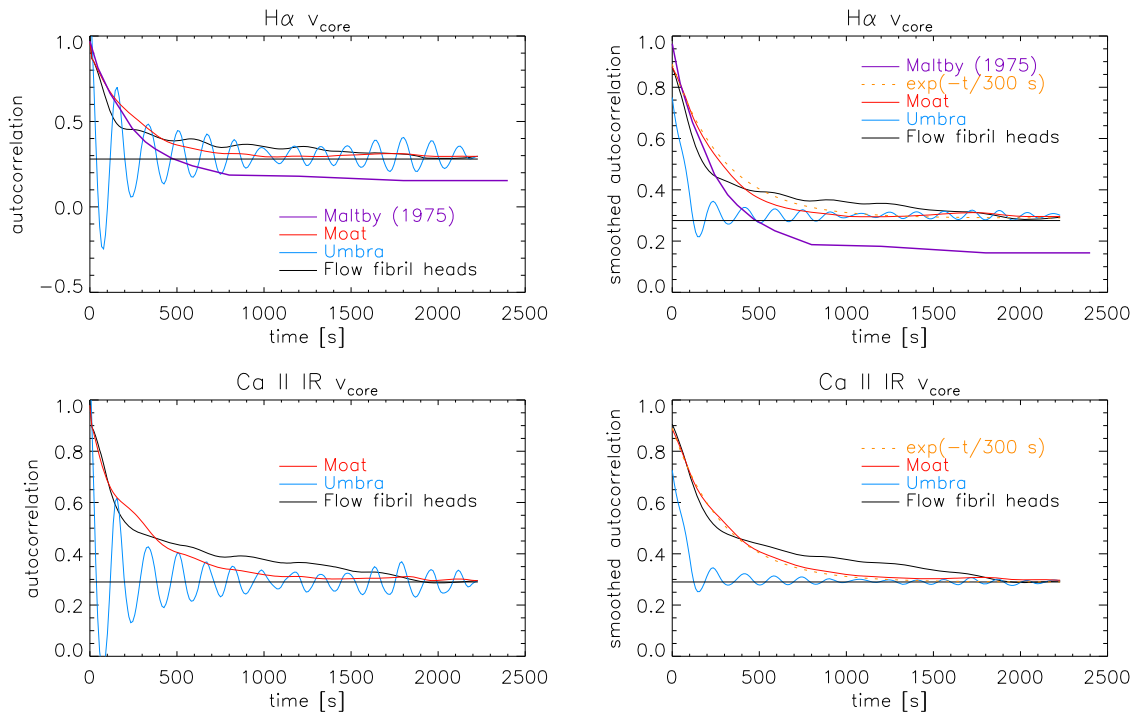


**Figure 8.** Auto-correlation times. Top row: temporal auto-correlation for the  $H\alpha$  LOS velocity in the IEF region (black line), the umbra (blue line), and the outer moat (red line) without (left panel) and with smoothing over the dominant period of the umbral oscillations (right panel). Bottom row: the same for Ca II IR. The orange dotted lines in the right column indicate a pure exponential decay with a time constant of 300 s. The purple line in the top row corresponds to the similar determination of temporal correlation in Maltby (1975), his figure 7.

lifetime of the IEF channels of several minutes and the temporal cadence of the observations of about 10 s, this does, however, not correspond to a sample of 10,000 different IEF channels, since many of them will be counted multiple times.

#### 4.2.1. Azimuth Angles

To determine the preferred azimuth locations of the IEF channels, we first averaged the radial cuts over the time series (see Figure 12). While the umbral oscillations average out completely both in the LOS velocity and the line-core intensity, several of the IEF channels that persist for a large fraction of the time still clearly stand out. There are no pronounced differences between  $H\alpha$  and Ca II IR apart from the somewhat higher contrast in the Ca II IR line-core intensity. The same is valid for the comparison of the FIRS He I data with the IBIS pseudo-scan maps in Figure 2.

We then averaged the velocities between the black horizontal lines in Figure 12 in the radial direction and determined the locations of IEF channels in azimuth by identifying local extrema—either minima or maxima—in the azimuthal direction (bottom panel of Figure 13). The same approach was applied to the radial cuts of each individual spectral scan (top panel of Figure 13). On average, about 35 IEF channels were found in the azimuthal direction in each spectral scan, while there were 32 IEF channels in the temporally averaged velocity map. Both spectral lines show similar LOS velocities and yielded about the same number of detected downflow points (Figure 13).

The locations of the IEF channels found in each spectral scan in Figure 14 confirm again the presence of IEF channels at the same place over several 10 minutes up to the full duration of the time series. It can also be seen that the lateral motion in azimuth is small and usually does not exceed  $2^\circ$ – $3^\circ$ . The

absence of IEF channels around  $60^\circ$  and  $240^\circ$  results from the lack of LOS velocities at those angles because of the projection effects.

Figure 15 shows the histogram of the azimuth angles at which IEF channels were found in the full time series. There are several angles with an increased probability of hosting IEF channels that naturally coincide with the locations of high velocities in the average azimuthal velocity variation (Figure 13) or the time-dependent determination (Figure 14) that exhibit the existence of the long-lasting IEF channels. The spacing between such preferred azimuthal locations is about  $10^\circ$  in the histogram, which is fully compatible with the average number of about 35 IEF channels found in each spectral scan under the assumption of equidistant spacing.

#### 4.2.2. Relation to MMFs

We only used a visual inspection of the aligned IBIS data and HMI magnetograms in Figure 1 to investigate a potential relation of the IEF channels and their evolution to MMFs in the moat around the sunspot, but there is no obvious connection between IEF channels and MMFs. On the one hand, the temporal scales of the evolution are completely off. The IEF channels change and evolve over less than 1 minute in some cases, while the MMFs in the FOV barely move by a few arcseconds over the full time series of 1 hour and also maintain their shape to the largest extent (e.g., compare the first and last panel of the bottom row of Figure 1). On the other hand, there are either almost no MMFs in the region with the most prominent IEF channels (black rectangle in Figure 1) at azimuth angles from  $270^\circ$  to  $360^\circ$  or the photospheric magnetic flux is comparably static (at azimuth angles from  $0^\circ$  to  $90^\circ$ ). Even thresholding the HMI magnetogram to lower magnetic

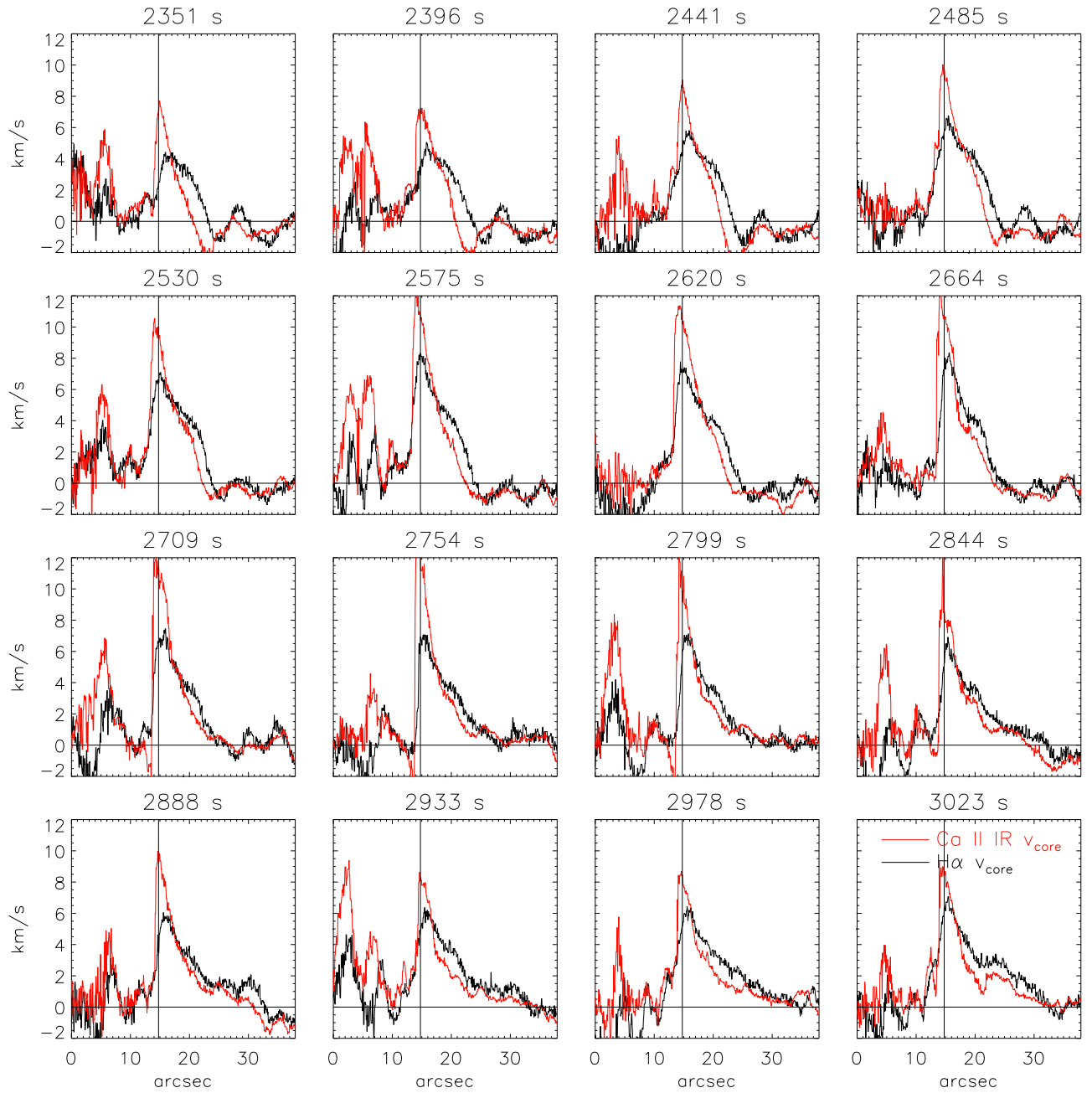


**Figure 9.** Temporal evolution of the LOS velocity at the start of an IEF channel at UT 15:21 at an azimuth angle of  $327^\circ$ . Black/red lines: LOS velocity of  $H\alpha$ /Ca II IR. The black vertical lines mark the location of maximum flow speed at the first time step. Time increases from top to bottom across rows and left to right in each row.

flux levels did not reveal any type of significant changes in the photospheric magnetic field in that area.

#### 4.2.3. Relation to Penumbral Magnetic Field

To determine a possible relation between the preferred azimuthal locations of IEF channels and the penumbral magnetic field, we averaged the HMI magnetic field results first over the duration of our observations and then over some radial range inside the penumbra. We applied the same identification of local extrema in  $B$ ,  $\gamma$ , and  $\Phi$  as used on the LOS velocities for the identification of IEF channels. The upper left panels of Figure 16 show the resulting azimuthal variation of  $B$ ,  $\gamma$ , and  $\Phi$  from HMI and the corresponding LOS velocity of  $H\alpha$  with the identified locations of local extrema in the

magnetic field properties overlaid on the  $H\alpha$  velocities. Even if there seems to be some overlap of locations with higher field strength or magnetic flux with the locations of IEF channels in the azimuthal curves, the connection is not convincing. The scatter plot of photospheric field strength against the chromospheric  $H\alpha$  velocity shows no trend at all (lower left panel of Figure 16), while the correlation between LOS magnetic flux  $\Phi$  and the LOS velocity of  $H\alpha$  (top panel in second column) just results from the common property of passing through zero and becoming maximal at the same azimuthal angles.

We repeated the same procedure with the FIRS Si I inversion results and the IBIS pseudo-scan maps to check if the lack of correlation might be related to the spatial resolution or polarimetric sensitivity. We obtained, however, the same result with no obvious relation between photospheric magnetic field

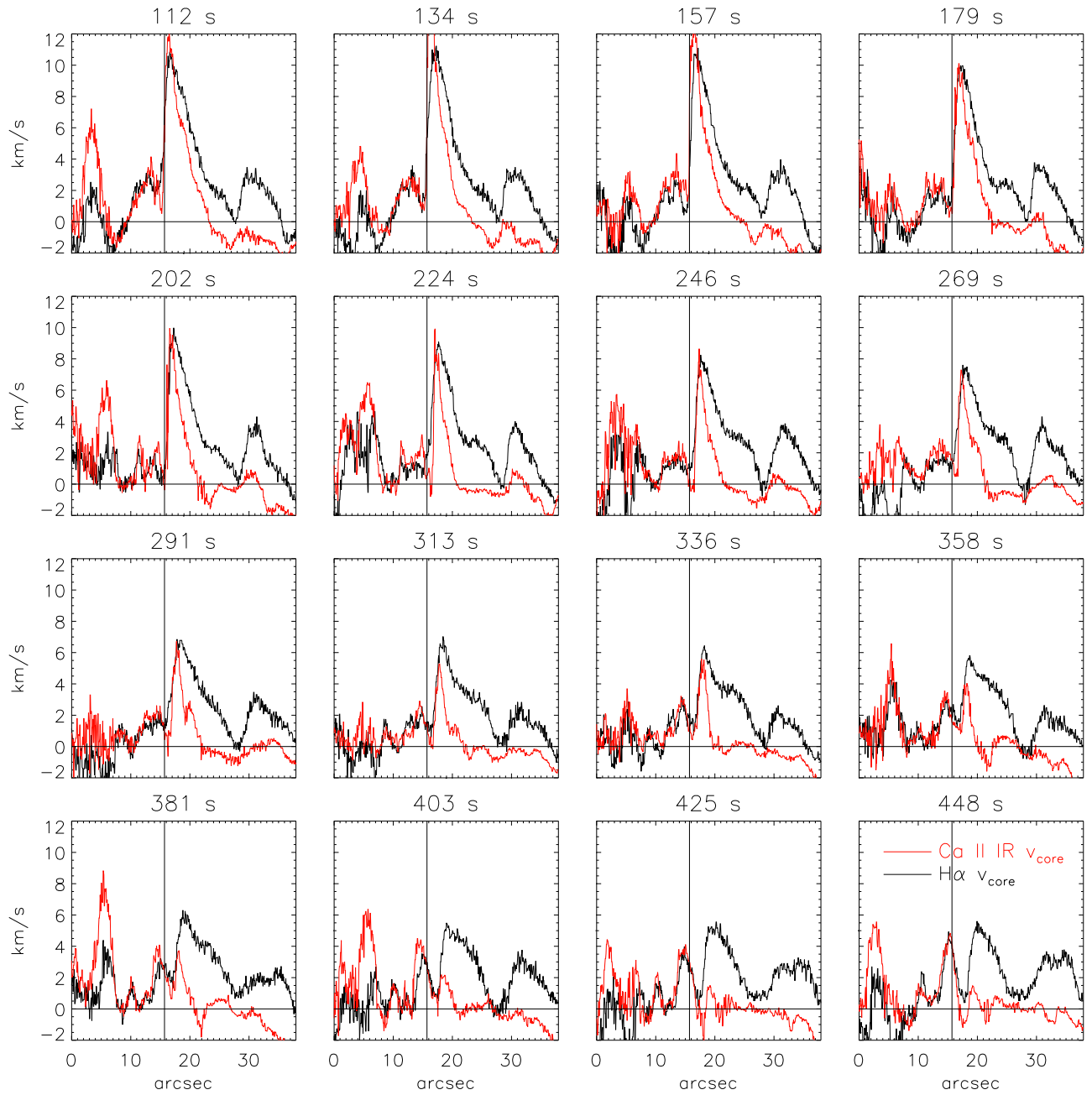


**Figure 10.** Temporal evolution of the LOS velocity at the end of an IEF channel at UT 14:44 at an azimuth angle of  $351^\circ$ . Black/red lines: LOS velocity of  $H\alpha$ / $Ca\ II\ IR$ . The black vertical lines mark the location of maximum flow speed at the first time step. Time increases from top to bottom across rows and left to right in each row.

properties and the preferred locations of the IEF channels (top-right panels of Figure 16), or in this case, even more clearly the actual absence of significant magnetic field variation at the preferred azimuthal locations of IEF channels. The characteristic azimuthal scale of variations in the photospheric penumbral field is also about  $10^\circ$  (e.g., the green line in the top-right panel of Figure 16), so any apparent cospatiality of IEF channels and local magnetic field strength maxima in azimuth could well be fully coincidental. The majority of the IEF downflow points are located inside the penumbra (see the next section).

#### 4.2.4. Radial Distance from the Spot Center

For the determination of the radial distance of the IEF channels from the sunspot center, we located the maximal velocity within the radial boundaries given in Figure 12. The maximal velocity within that radial range is usually found at the end of an IEF channel (Figures 9 and 10). The bottom panel of Figure 17 shows the histogram of the radial distances and the top panel the average value with azimuth angle. The limb and center side were treated separately to take the difference between them due to the projection effects into account. The IEF downflow points are found to lie from 0.6 to 1.4 spot radii on the center side, with a maximum probability of occurrence within the penumbra at around  $0.9 \pm 0.14$  spot radii. For the limb side, the locations shift beyond the outer penumbral

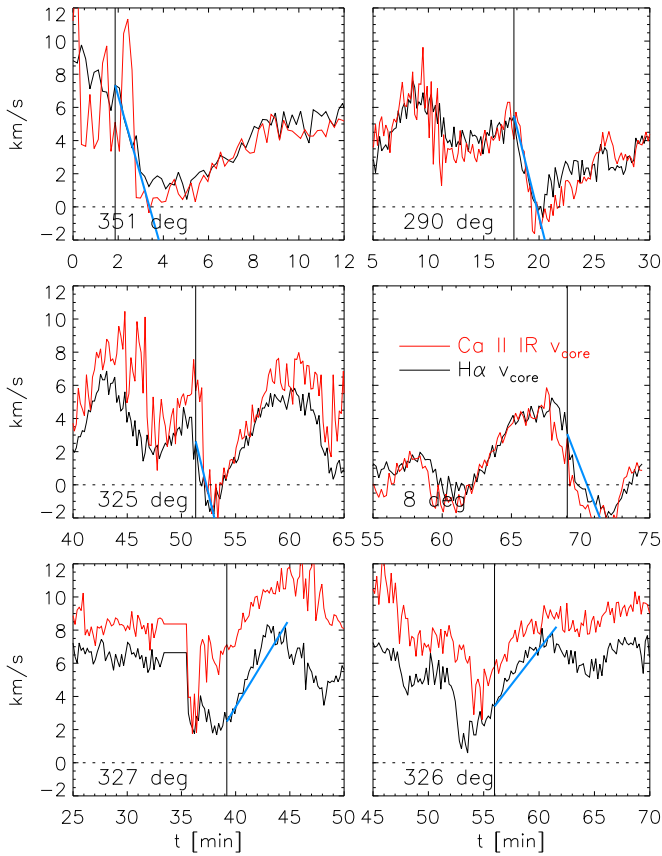


**Figure 11.** Temporal evolution of the LOS velocity at the start (bottom row) and end (top two rows) of IEF flow channels. Black/red lines: LOS velocity of H $\alpha$ /Ca II IR. The black vertical lines mark the assumed time of the onset of the change of flow speed. The inclined blue lines indicate the acceleration and deceleration, respectively.

**Table 1**  
Acceleration and Deceleration of IEF Speed

Angle (deg)	351	290	325	8	327	326	...
$a$ ( $\text{m s}^{-2}$ )	-80	-45	-45	-36	18	14	45 <sup>a</sup>
0–8 $\text{km s}^{-1}$ (s)	100	179	179	224	448	560	179 <sup>a</sup>

**Note.**

<sup>a</sup> Derived from Montesinos & Thomas (1993).

boundary and the probability monotonically increases with increasing radial distance. These values are, however, strongly biased by the location of the symmetry line of the sunspot that reduces the LOS velocities at the expected true location of the IEF downflow points to zero, and by the presence of the large-scale, curved, and permanently present filaments on the limb side of the sunspot (see Figure 1).

As an independent determination of the radial location of the downflow points, we also directly averaged the LOS velocities and line-core intensities over time. Figure 18 shows the radial variation of the H $\alpha$  and Ca II IR velocities and intensities separately for the limb and center side. The same difference between limb and center side as before is found with the maximal flow velocity further out on the limb side. The line-core intensities are less affected by the projection effects, as there is no symmetry line for intensity. The downflow points with increased intensity are therefore found closer to the penumbra on the limb side as well. We note that the H $\alpha$

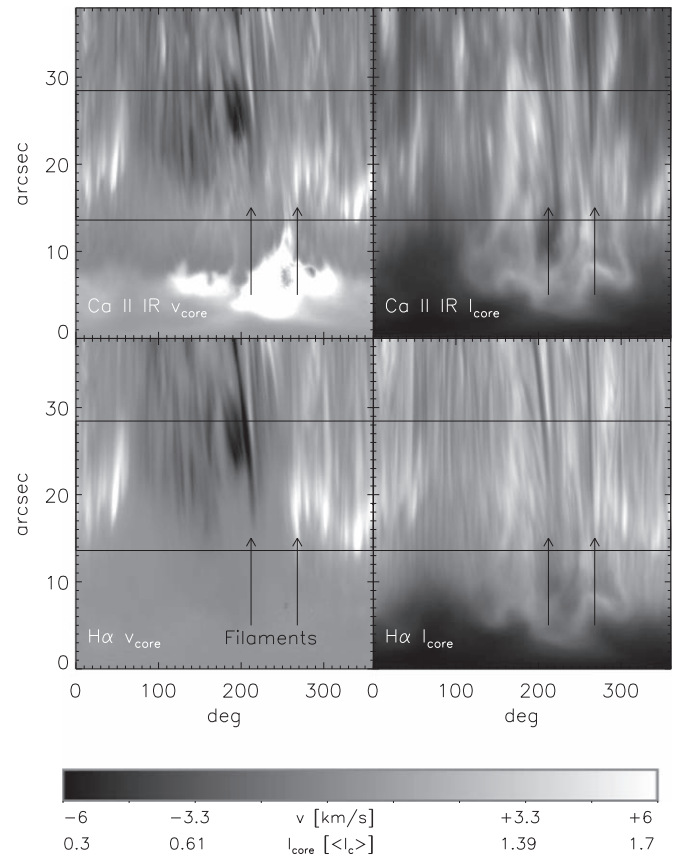


**Figure 12.** Temporal average over the time series. Bottom (top) row, left to right: line-core intensity and velocity of H $\alpha$  (Ca II IR). The horizontal black lines indicate the radial range used for the determination of the location of IEF channels. The black vertical arrows mark the locations of the two strongest super-penumbral filaments in the FOV.

intensity also shows a radial intensity maximum at about the sunspot boundary and thus must be sensitive to temperature effects to some extent.

### 4.3. Resolved H $\alpha$ , Ca II IR, and He I Spectra

In Paper I, we found that the IEF channels do only show up as a strongly Doppler-shifted line satellite close to the downflow points. Tests with synthetic data suggested that this results even for an assumed flow channel with 100% fill factor in the upper atmosphere, which would indicate a vertical structuring along the LOS. To cross-check whether it still possibly could be caused by the limited spatial resolution of  $>0''.7$  of the SPINOR data used in Paper I, we extracted a similar set of individual spectra along an IEF channel from the current data sets. Figure 19 shows H $\alpha$ , Ca II IR, and He I spectra on a cut along a flow fibril that intersected the downflow point. For the IBIS data in H $\alpha$  and Ca II IR, we obtain the same general picture as before with a strong component at rest and a weak line satellite in the red line wing with large LOS velocities. The spectra of the He I line at 1083 nm differ to some extent, but upstream of the downflow point. For He I the unshifted component is missing or weaker than the Doppler-shifted one there. Beyond the downflow point the pattern changes to the same as in the other lines, with the Doppler-shifted component getting weaker the larger the Doppler shift and the closer to the umbra the spectrum was recorded. The pattern in all lines therefore still would comply

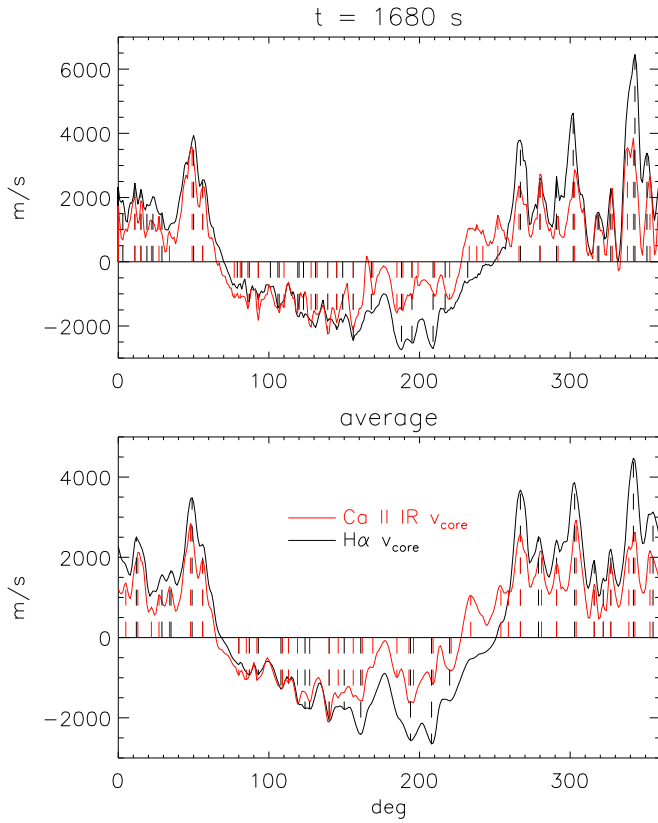


**Figure 13.** Determination of the location of IEF channels in azimuth angle. Bottom panel: determination of local velocity extrema in the temporal average. Black/red solid lines: temporal average of the velocity in  $H\alpha$  and  $Ca II IR$  spatially averaged between the two black lines in Figure 12. Black/red vertical dashed lines: identified locations of enhanced flow speeds in  $H\alpha$  and  $Ca II IR$ . Top panel: the same for an individual spectral scan with only the spatial averaging.

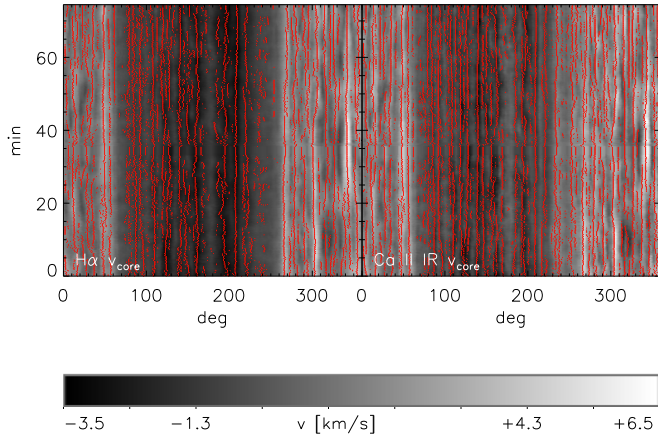


**Figure 14.** Locations of IEF channels with azimuth and time. Left/right panel: LOS velocity of  $H\alpha$  and  $Ca II IR$  for each spectral scan averaged between the two black lines in Figure 12. Red dots: identified locations of local velocity extrema.

with a vertical structuring, where for  $He I$  there is no absorbing matter of high opacity apart from the IEF channel radially outwards from the downflow point.

## 5. Summary

We investigated a time series of  $H\alpha$  and  $Ca II IR$  spectra of about 1 hour duration and a spatial map in the  $He I$  line at

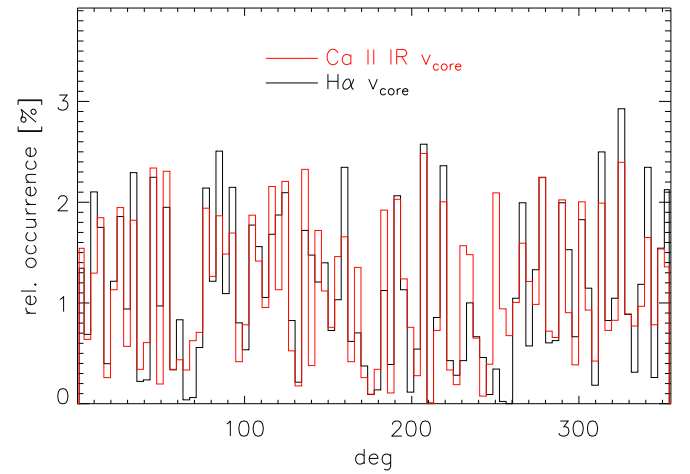


**Figure 15.** Histogram of the azimuth angles of IEF channels. Black/red line: derived from the velocity of  $H\alpha$  and  $Ca II IR$ .

1083 nm to infer the temporal evolution of the IEF. All three chromospheric lines show a very similar behavior in their line-core intensity and the LOS velocity with matching spatial and temporal properties. We find that individual IEF channels persist for a few ten minutes to more than 1 hour. IEF channels that disappear are often rapidly replaced by a new channel at about the same location after a short time. The IEF channels show little radial or lateral motion and usually end in the mid-to outer penumbra. Initiation of the flow takes about 10 minutes, while the termination is faster and takes only about 5 minutes. The IEF channels seem to appear at preferred azimuth angles that are spaced at about  $10^\circ$  distance. We cannot find any clear relation of the locations of the IEF channels to local variations or specific properties of the photospheric penumbral magnetic field, nor any causal connection of the IEF channels to MMFs outside of the sunspot. Several more transient processes that can be seen in the time series were not studied in full detail, but in general seem to have only little impact on the structure and evolution of the IEF channels.

## 6. Discussion

Our current results are in line with the findings of Paper I and of most previous literature.

### 6.1. Structure of the IEF

We find no significant difference between the appearance of the IEF channels in the three chromospheric lines of  $He I$  at 1083 nm,  $Ca II IR$  at 854 nm, and  $H\alpha$  at 656 nm. All spectra and the derived quantities comply with a picture of IEF channels as flow fibrils at chromospheric levels that turn down to the photosphere at the inner end point in the penumbra, where a shock forms because of the supersonic flow speed. Even at the improved spatial resolution as compared with Paper I, the IEF channels show up as a Doppler-shifted line satellite close to the downflow points. This suggests a vertical structuring along the LOS instead of lateral spatial resolution effects.

Averaged flow speeds of about  $4 \text{ km s}^{-1}$  (Figure 18) match the results of  $4\text{--}6 \text{ km s}^{-1}$  in, for instance, Dialelis et al. (1985) or Georgakilas et al. (2003). Thanks to the higher spatial and spectral resolution of our data, we can demonstrate that the true LOS velocities of individual IEF channels are two to four times

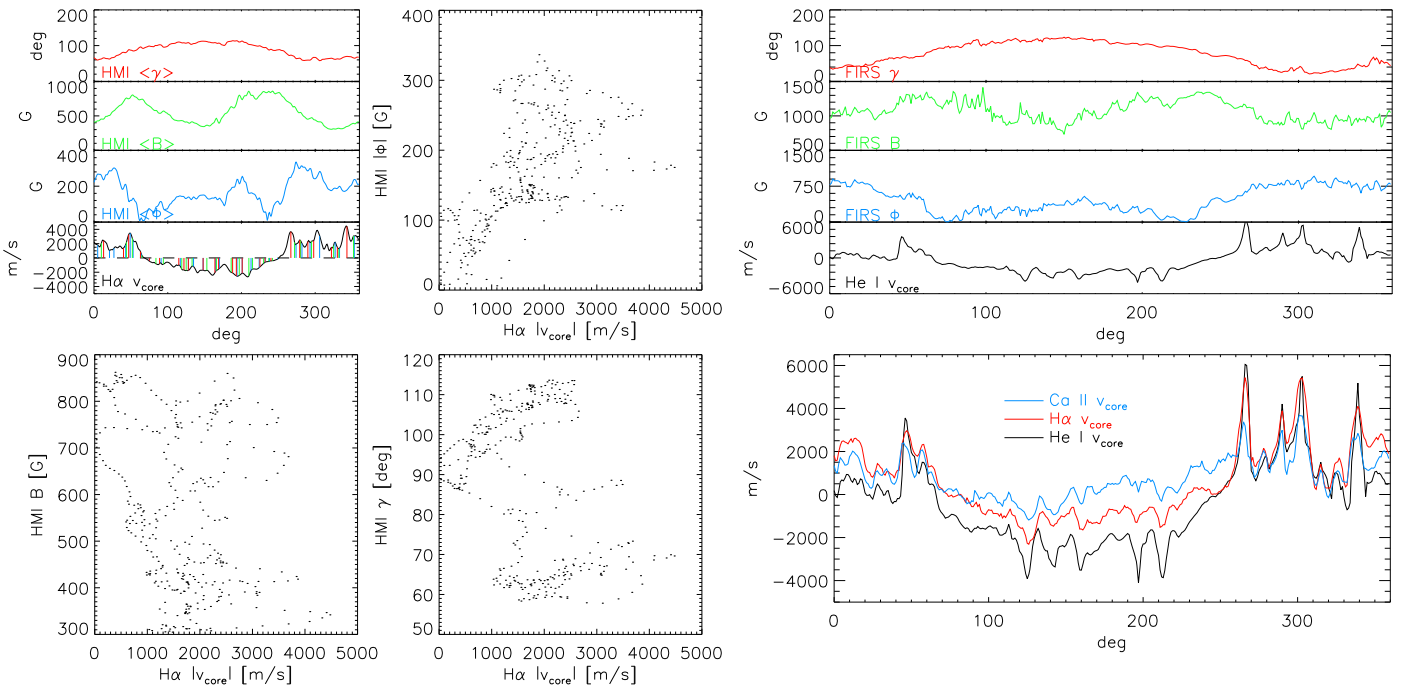


**Figure 16.** Relations between IEF channel locations and penumbral magnetic field properties. Left four panels, top-left: spatially and temporally averaged LOS velocity of H $\alpha$  (black line), HMI LOS magnetic flux  $\Phi$  (blue line), HMI magnetic field strength  $B$  (green line), and HMI magnetic field inclination  $\gamma$  (red line). The vertical red, green, and blue colored lines in the H $\alpha$  velocity indicate the locations of local extrema in  $\gamma$ ,  $B$ , and  $\Phi$ . Left four panels, top-right and bottom row: scatter plots of  $\Phi$ ,  $B$ , and  $\gamma$  against the LOS velocity of H $\alpha$ . Rightmost column, bottom panel: spatially averaged LOS velocities of He I (black line), and from the pseudo-scan of H $\alpha$  (red line) and Ca II IR (blue line). Rightmost column, top panel: He I LOS velocity (black line), LOS magnetic flux  $\Phi$  (blue line), magnetic field strength  $B$  (red line), and inclination  $\gamma$  (green line) from the SIR inversion of Si I at 1082.7 nm.

as high, which makes them supersonic at photospheric heights already without additionally taking the projection effects onto the LOS into account. The radial locations of the downflow points inside the penumbra or close to the outer penumbral boundary also match previous findings (Dialetis et al. 1985; Alissandrakis et al. 1988; Dere et al. 1990; Georgakilas et al. 2003). We were not able to find any clear connection of the IEF channels in general or downflow points in specific to the local photospheric magnetic field properties or its temporal evolution neither in the penumbra nor in the moat, even if the IEF channels seem to occur repeatedly at preferred azimuthal angles around the sunspot center. Joshi et al. (2016) found a similar lack of a strong correlation between chromospheric flows and in their case the chromospheric magnetic field vector.

The pronounced difference between LOS velocities on the center and limb side of the sunspot will be primarily due to the projection effects (left half of Figure 20) at the heliocentric angle of the observations of  $43^\circ$ . Assuming field-aligned flows, the LOS is about perpendicular to the flow direction just where the IEF downflow points on the limb side would be. This is confirmed by the presence of an enhanced line-core intensity on the limb side at about the same radial distance as on the center side because the intensity is barely impacted by the LOS effects.

## 6.2. Temporal Evolution of the IEF

Our findings on the temporal evolution of the IEF channels closely follow those of Maltby (1975) and Georgakilas & Christophoulou (2003). The lifetime of individual IEF channels is of a few to upward of 10 minutes, while some last for the full duration of the observations of more than 1 hour. Similar to the description of Maltby (1975), we see occurrences of IEF

channels getting replaced by new ones at about the same location. An established IEF channel persists with about the same properties for several minutes with little radial or lateral motion and without any clear impact of the transient events discussed in the next section. The IEF channels are clearly not oscillatory phenomena. In the few cases, where we could track the start and stop of individual isolated IEF channels, we find that the initial acceleration over up to about 10 minutes takes about twice as long as the deceleration at the end. Accelerations are on the order of a few ten  $\text{m s}^{-2}$  and fall short of gravitational acceleration in free fall.

## 6.3. Relation of IEF and Transient Events

Our observations had a higher spatial, spectral, and temporal resolution than most previous data used for similar studies on the IEF. This allowed us a much clearer distinction between the IEF channels and other more transient phenomena that can clearly be seen to be present in the animation of the observation and multiple plots, but were not investigated in detail in the current study.

### 6.3.1. IEF Channels and RPWs

From a preliminary analysis of RPW (see, e.g., Giovanelli 1972; Zirin & Stein 1972; Briskin & Zirin 1997; Bloomfield et al. 2007; Jess et al. 2013; Priya et al. 2018, and citations and references therein) events in our data, we found that their maximal LOS velocity amplitude is only about  $1 \text{ km s}^{-1}$  in and near the umbra. The amplitude of the RPWs decays rapidly with radial distance (lower row of Figure 4). At the location of the IEF downflow points, the IEF velocity is usually about an order of magnitude larger than that of the RPWs. In the animation of the observations, especially in the

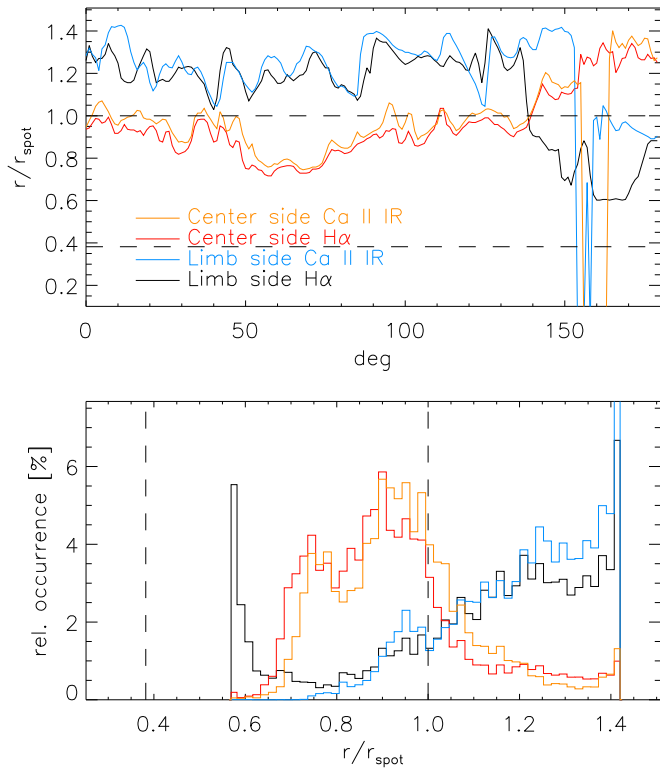


**Figure 17.** Radial distance of maximal flow velocities from the sunspot center. Top panel: temporal average of the radial distance of the location of maximal velocity between the two black lines in Figure 12 in each spectral scan at each azimuth angle. Black/blue lines: derived from the LOS velocity of  $H\alpha$  and Ca II IR on the limb side. Red/orange lines: derived from the LOS velocity of  $H\alpha$  and Ca II IR on the center side. Bottom panel: histograms of the radial distance derived from the same quantities as above. The two black dashed lines indicate the umbral and penumbra boundary.

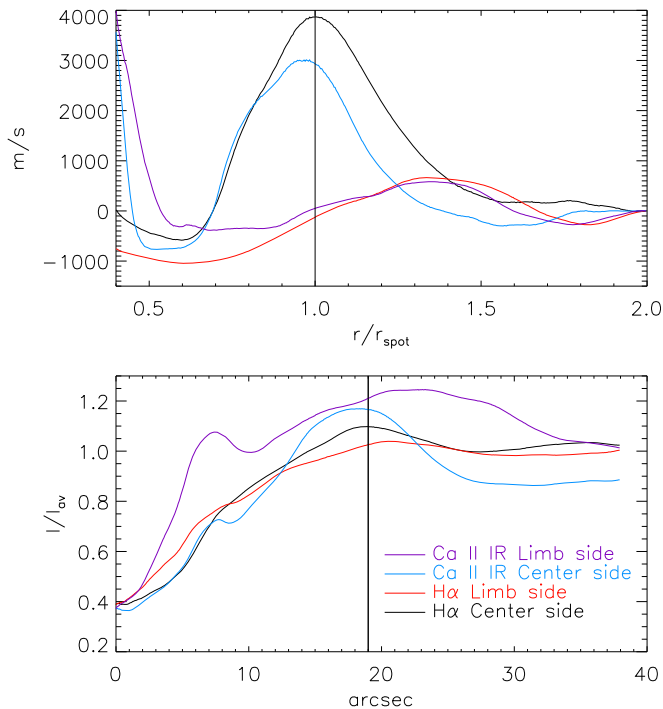


**Figure 18.** Average radial intensities (bottom row) and velocities (top row). Black and red lines:  $H\alpha$  on center and limb side. Blue and purple lines: Ca II IR on center and limb side. The vertical black lines indicate the outer penumbral boundary located at about  $19''$ .

temporal and azimuthal derivative of the  $H\alpha$  LOS velocity, it can be seen that the RPWs that initially arrive as a spatially extended wavefront at the umbral boundary tend to split into multiple threads, some of which run along existing IEF channels. The IEF channels, however, persist without any visible change throughout multiple such events. We thus do not see any direct influence of RPWs on the IEF channels, also not in connection with the start and stop of an IEF channel.

### 6.3.2. IEF Channels and Velocity Packets

A second feature that we did not investigate in more detail are the events labeled “velocity packets” by Georgakilas & Christophoulou (2003). They consist of two types, small roundish patches of a LOS velocity with an opposite sign to the IEF located between the IEF downflow points and the umbra and elongated fibril-like patches radially outward from the downflow points (seen as black color inside the black rectangle in the LOS velocity maps of Figure 1 and the animation). The roundish patches sometimes propagate radially outwards through the IEF downflow points and convert to the second type of elongated features. The latter seem to always move away from the sunspot.

Again, a preliminary analysis confirmed generally velocity amplitudes much smaller than those of the IEF channels. Similar to their reaction to RPWs, IEF channels also persist without any clear change when such velocity packets pass through or along them. Even looking at individual cases did not make it obvious what the actual physical process is that leads to the velocity packets. The elongated type outwards of the IEF downflow points gives the impression of rising loops or field lines in some cases. The evolution of the velocity packets is generally much faster than that of the IEF channels.

Given the lack of a clear relation to the photospheric magnetic field structure and evolution in and close to the sunspot, we suggest that the primary driver governing the temporal evolution of IEF channels could be located at the outer end of the IEF channels in the sunspot moat instead. A reconfiguration of the magnetic field at the outer end could generate the conditions for the initialization or termination of the flow along specific IEF channels. The velocity packets could actually be related to such a process when they reach the outer end of the moat flow, but this requires further study.

### 6.4. Relation to Global Sunspot Structure

Figure 20 attempts to put our results on the IEF structure and evolution from Choudhary & Beck (2018), Beck & Choudhary (2019), and the current study into the larger picture of sunspot topology and dynamics.

The results on the inclined flow angle (Haugen 1969; Dialelis et al. 1985; Georgakilas et al. 2003; Beck & Choudhary 2019) and the direction opposite to the photospheric EF require that the IEF connects to a different set of magnetic field lines than those that harbor the nearly horizontal EF (right panel of Figure 20). Those field lines would have to reach chromospheric heights in or close to the penumbra, continue throughout the super-penumbra in or close to the chromosphere—because the IEF channels can be identified over several Mms in the radial direction outside of the penumbra—and then connect to places presumably at the end of the moat cell. MMFs would correspond to photospheric structures below the IEF channels that would connect to the

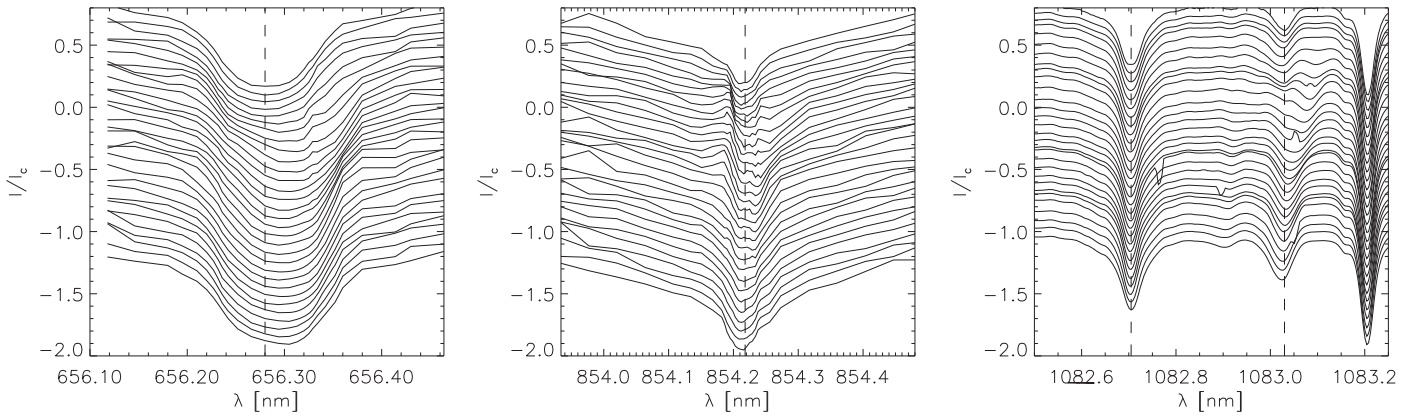


**Figure 19.** Example spectra of H $\alpha$  (left panel), Ca II IR (middle panel), and He I at 1083 nm (right panel) along an IEF channel around the downflow point. The dashed black vertical lines indicate the rest wavelength of the spectral lines. The downflow point is located in the upper part at a relative intensity of about zero and the umbra is toward the top of the panels.

horizontal magnetic field lines of the EF instead (Cabrera Solana et al. 2006). Umbral field lines would only reach the photosphere again at much larger distances from the sunspot and with much larger apex heights, which could render it impossible to drive a siphon flow along them. This topology would imply that EF and IEF are two distinct, unrelated phenomena with eventually different physical drivers.

As far as the radial propagation of umbral waves (UWs) and RPWs is concerned, our data suggest that they most likely result from coherent oscillations across the whole sunspot cross-section below the photosphere. Each RPW in Figure 4 has an associated UW (see also Tziotziou et al. 2006). The apparent radial propagation speed of the UWs is  $100 \text{ km s}^{-1}$  or more, with in some case zero slope of the UW phase ridges in the  $r$ - $t$ -diagram, which would imply infinite speed. A wave source below the surface across the whole sunspot cross-section would be able to consistently explain both the UW and RPW speeds, where the latter show an only apparent radial propagation caused by an increased time delay when reaching the chromosphere because of the longer distance to be traveled along the inclined penumbral magnetic field lines (orange arrows in the left panel of Figure 20; Bloomfield et al. 2007).

### 6.5. Possible Drivers of the IEF

As noted in our previous publications (Choudhary & Beck 2018; Beck & Choudhary 2019), the observed properties of the IEF are compatible with a siphon flow mechanism (see, e.g., Thomas 1988, and references therein). Here, we give a brief updated account of the properties of the IEF adding the results from the current study. We observed the persistent existence of IEF channels in the line core of the Ca II IR line at 854.2 nm that has a formation height of about  $1 \pm 0.2 \text{ Mm}$ . The IEF is found only along the elevated chromospheric fibrils and absent outside. The flow angle is inclined  $30^\circ$ - $90^\circ$  to the local surface normal near the downflow points. The chromospheric fibrils join the outer penumbra with the surrounding super-penumbral boundary that hosts more diffuse photospheric magnetic elements. The flows terminate at the penumbral end of the fibrils, where the downflowing material creates a stationary shock front with enhanced temperatures of up to 2000 K above quiet Sun conditions. There are no indications of significant downflows at the presumed outer end of the flow fibrils. The photospheric magnetic fields strength at the downflow points that are located mostly at the outer

penumbral boundary is greater than 1 kG. In the current study, we find that the flows are stationary over about ten minutes to more than 1 hour. There are no indications of significant changes of the magnetic field topology like magnetic flux emergence in the moat in the photospheric magnetic field measurements or permanently rising loops in the chromospheric diagnostics.

Let us consider several mechanisms proposed to explain the downward flow of material toward the surface of the Sun. One of the mechanisms is due to rising loops in which the material at the loop top is condensing and subsequently drains due to gravitational forces (Beckers 1962). In this situation, downflows should be observed at both ends of the loop which would last for a comparably short period because of the limited mass reservoir in the loop. This is contrary to our findings: the lifetime of the flows reported here is several 10s of minutes, which cannot be maintained by rising loops with chromospheric densities, and we do not detect systematic downflows at the outer end of the fibrils. Furthermore, the temporal evolution of the HMI magnetograms and the chromospheric intensity and velocity maps do not indicate any rise of existing magnetic flux or new magnetic flux emergence, especially not in the shape of the radial thin elongated structures of several Mm length that would be required. Given the limited formation height of the Ca II IR line core, rising loops would have to be constantly replenished from below to maintain the persistent existence of the fibrils in that line.

Another mechanism to drive flows is the so-called moving tube model (Montesinos & Thomas 1997; Schlichenmaier et al. 1998b), in which the flow is driven by the gas pressure difference between a hot upflow point and the colder outer end. The flow direction is radially outward from a point with higher to lower magnetic field strength. This mechanism was suggested to be responsible for the photospheric Evershed flow. Its properties are, however, again at odds with our results for the IEF channels. We found that the temperature at the inner end is up to 2000 K above QS conditions. If the temperature at the outer end would not be even significantly higher than that, a flow driven by the thermal gas pressure difference would go in the opposite direction to the observed IEF.

Observations of coronal rain (Vissers & Rouppe van der Voort 2012; Ahn et al. 2014) show a much more both spatially and temporally intermittent behavior than the long-lived IEF channels along the elongated thin flow and intensity fibrils.

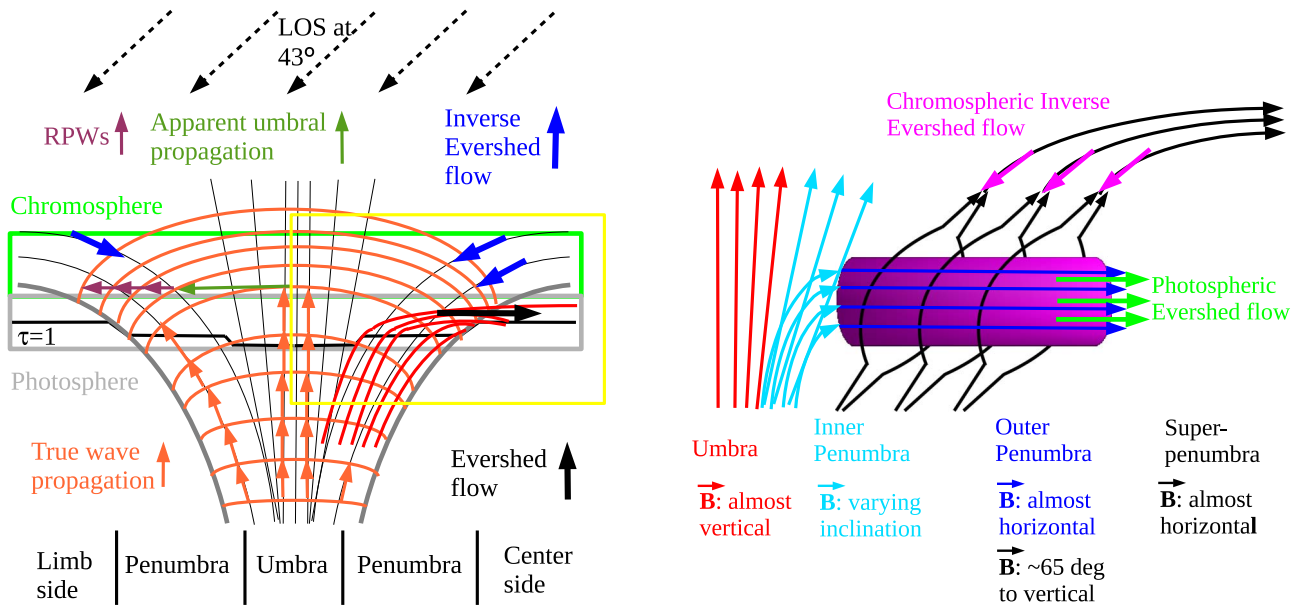


**Figure 20.** Sketch of the magnetic topology of a sunspot and the various wave and flow phenomena. Left panel: side view of a sunspot. The gray and green rectangles indicate photosphere and chromosphere. Gray and red lines indicate magnetic field lines. Orange lines and arrows show the wavefront and assumed propagation of global sunspot oscillations. Black and blue arrows highlight the direction of the EF and IEF. The apparent radial propagation of umbral and penumbral waves is indicated by green and purple arrows. Right panel: magnification of the assumed magnetic field vector and the flows in the penumbra inside the yellow rectangle of the left panel.

Oscillations from inside the sunspot were found to have almost zero velocity amplitude at the locations of the IEF downflow points in the current study.

We thus do not think that any proposed option apart from a siphon flow mechanism is valid to explain the IEF. A definite proof requires the explicit measurement of the field strength at the outer end points. The biggest limitation here is that the IBIS FOV is 90'' in diameter. For a sunspot as large as the one in the current study, the magnetic network elements at the outer end of the moat cell are not covered (see, e.g., the HMI magnetogram in Figure 1), apart from the question how well one can really uniquely determine the more diffuse outer end of the IEF channels. To fully understand the formation of IEF channels and their intermittent nature would require a combination of chromospheric and photospheric diagnostics with high spatial and temporal resolution over an even larger FOV to track both the flow fibrils and the photospheric magnetic field up to the end of the moat cell.

For the interpretation of the IEF in the current study, we would argue that none of the other proposed drivers matches all of the observed IEF properties, while none of the observed properties is at odds with a siphon flow mechanism.

### 6.6. Future Work

Apart from the topics on the transient phenomena that merit further investigation, we would like to point out some more avenues that could be pursued on the IEF itself.

The detailed relation between the EF and IEF, or its absence, requires simultaneous information on photospheric and chromospheric layers. The different bisector levels in our analysis, which we did not actually make use of in the current study, would allow one to trace EF, IEF, and wave phenomena with height in the atmosphere, but only within limits. A combination of quasi-simultaneous photospheric and chromospheric observations would be better suited. Of especial interest would be the search for any possible relation between the IEF downflow

points and photospheric downflows in the penumbra (Katsukawa & Jurčák 2009, 2010). The IEF downflow points are well localized and the flow speed is not zero after the deceleration by the stationary shock (Paper I), so there is mass that should reach the photosphere, but only at a few well-defined places. An in-depth analysis of the height variation of thermal and dynamic properties would also benefit from more sophisticated approaches in the analysis of the spectra by means of an inversion of the Ca II IR and H $\alpha$  spectra (Beck et al. 2019; Schwartz et al. 2019).

Another topic of interest would be to track the evolution at the outer end of IEF channels in or at the end of the moat cell. We were unable to identify trigger events that control the start or end of the IEF channels at the inner end point within the limits of the spatial resolution of our polarimetric data. Such data would require an FOV that covers both ends of the IEF channels in one go at a spatial resolution similar to that of the IBIS data used here, but including spectropolarimetry.

## 7. Conclusions

We find that the IEF happens along long-lived (10–60 minutes) super-penumbral fibrils that show little evolution over their lifetime. The IEF is no oscillatory phenomenon but a stationary flow along arched magnetic field lines that connect the outer penumbra with locations in or at the end of the sunspot moat. We did not find any relation of individual IEF channels to specific local photospheric magnetic field properties in the penumbra or to MMFs outside of the sunspot. Fully in line with our previous results, we propose that the IEF is driven by a siphon flow mechanism. At the spatial resolution of our polarimetric data and the FOV of the chromospheric diagnostics, we cannot definitely determine if the events that govern the start or termination of IEF channels do happen at the outer end of the flow channels in the moat or at the inner end in the penumbra.

The Dunn Solar Telescope at Sacramento Peak/NM was operated by the National Solar Observatory (NSO). NSO is operated by the Association of Universities for Research in Astronomy (AURA), Inc., under cooperative agreement with the National Science Foundation (NSF). IBIS has been designed and constructed by the INAF/Osservatorio Astrofisico di Arcetri with contributions from the Università di Firenze, the Università di Roma Tor Vergata, and upgraded with further contributions from NSO and Queens University Belfast. HMI data are courtesy of NASA/*SDO* and the HMI science team. This work was supported through NSF grant AGS-1413686. We thank the referee for his comments and suggestions. We thank S. Gosain (NSO) and S. Crisculi (NSO) for helpful comments on the paper.

### ORCID iDs

C. Beck  <https://orcid.org/0000-0001-7706-4158>

D. P. Choudhary  <https://orcid.org/0000-0002-9308-3639>

### References

- Ahn, K., Chae, J., Cho, K.-S., et al. 2014, *SoPh*, **289**, 4117
- Alissandrakis, C. E., Dialetis, D., Mein, P., Schmieder, B., & Simon, G. 1988, *A&A*, **201**, 339
- Antia, H. M., Chitre, S. M., & Gokhale, M. H. 1978, *SoPh*, **60**, 31
- Bard, S., & Carlsson, M. 2008, *ApJ*, **682**, 1376
- Beck, C. 2006, PhD thesis, Albert-Ludwigs-Univ. <http://www.freidok.uni-freiburg.de/volltexte/2346/>
- Beck, C. 2008, *A&A*, **480**, 825
- Beck, C., Bellot Rubio, L. R., Schlichenmaier, R., & Sütterlin, P. 2007, *A&A*, **472**, 607
- Beck, C., & Choudhary, D. P. 2019, *ApJ*, **874**, 6
- Beck, C., Gosain, S., & Kiessner, C. 2019, *ApJ*, **878**, 60
- Beck, C., & Rezaei, R. 2009, *A&A*, **502**, 969
- Beck, C., Rezaei, R., & Fabbian, D. 2011, *A&A*, **535**, A129
- Beckers, J. M. 1962, *AuJPh*, **15**, 327
- Beckers, J. M., & Tallant, P. E. 1969, *SoPh*, **7**, 351
- Bloomfield, D. S., Lagg, A., & Solanki, S. K. 2007, *ApJ*, **671**, 1005
- Boerner, P., & Kneer, F. 1992, *A&A*, **259**, 307
- Bones, J., & Maltby, P. 1978, *SoPh*, **57**, 65
- Borrero, J. M., Solanki, S. K., Bellot Rubio, L. R., Lagg, A., & Mathew, S. K. 2004, *A&A*, **422**, 1093
- Brisken, W. F., & Zirin, H. 1997, *ApJ*, **478**, 814
- Cabrera Solana, D., Bellot Rubio, L. R., Beck, C., & del Toro Iniesta, J. C. 2006, *ApJL*, **649**, L41
- Cavallini, F. 2006, *SoPh*, **236**, 415
- Choudhary, D. P., & Beck, C. 2018, *ApJ*, **859**, 139, (Paper I)
- Dere, K. P., Schmieder, B., & Alissandrakis, C. E. 1990, *A&A*, **233**, 207
- Dialetis, D., Mein, P., & Alissandrakis, C. E. 1985, *A&A*, **147**, 93
- Dunn, R. B. 1969, *S&T*, **38**, 368
- Dunn, R. B., & Smartt, R. N. 1991, *AdSpR*, **11**, 139
- Evershed, J. 1909a, *MNRAS*, **69**, 454
- Evershed, J. 1909b, *Obs*, **32**, 291
- Felipe, T., Khomenko, E., Collados, M., & Beck, C. 2010, *ApJ*, **722**, 131
- Franz, M., & Schlichenmaier, R. 2009, *A&A*, **508**, 1453
- Georgakilas, A. A., & Christopoulou, E. B. 2003, *ApJ*, **584**, 509
- Georgakilas, A. A., Christopoulou, E. B., Skodras, A., & Koutchmy, S. 2003, *A&A*, **403**, 1123
- Giovanelli, R. G. 1972, *SoPh*, **27**, 71
- Grant, S. D. T., Jess, D. B., Zaqarashvili, T. V., et al. 2018, *NatPh*, **14**, 480
- Haugen, E. 1969, *SoPh*, **9**, 88
- Hirzberger, J., & Kneer, F. 2001, *A&A*, **378**, 1078
- Houston, S. J., Jess, D. B., Asensio Ramos, A., et al. 2018, *ApJ*, **860**, 28
- Ichimoto, K., Shine, R. A., Lites, B., et al. 2007, *PASJ*, **59**, 593
- Jaeggli, S. A., Lin, H., Mickey, D. L., et al. 2010, *MmSAI*, **81**, 763
- Jess, D. B., Morton, R. J., Verth, G., et al. 2015, *SSRv*, **190**, 103
- Jess, D. B., Reznikova, V. E., Van Doorslaere, T., Keys, P. H., & Mackay, D. H. 2013, *ApJ*, **779**, 168
- Johannesson, A. 1993, *A&A*, **273**, 633
- Joshi, J., Lagg, A., Solanki, S. K., et al. 2016, *A&A*, **596**, A8
- Katsukawa, Y., Berger, T. E., Ichimoto, K., et al. 2007, *Sci*, **318**, 1594
- Katsukawa, Y., & Jurčák, J. 2009, in ASP Conf. Ser. 415, The Second Hinode Science Meeting: Beyond Discovery-Toward Understanding, ed. B. Lites et al. (San Francisco, CA: ASP), 117
- Katsukawa, Y., & Jurčák, J. 2010, *A&A*, **524**, A20
- Khomenko, E., & Collados, M. 2015, *Lrsp*, **12**, 6
- Kjeldseth-Moe, O., Brynildsen, N., Brekke, P., Maltby, P., & Brueckner, G. E. 1993, *SoPh*, **145**, 257
- Krishna Prasad, S., Jess, D. B., & Khomenko, E. 2015, *ApJL*, **812**, L15
- Kuckein, C., Martínez Pillet, V., & Centeno, R. 2012, *A&A*, **539**, A131
- Kurucz, R. L., Furenliid, I., Brault, J., & Testerman, L. 1984, Solar Flux Atlas from 296 to 1300nm (Sunspot, NM: National Solar Observatory)
- Louis, R. E., Beck, C., & Ichimoto, K. 2014a, *A&A*, **567**, A96
- Louis, R. E., Beck, C., Mathew, S. K., & Venkatakrishnan, P. 2014b, *A&A*, **570**, A92
- Maltby, P. 1975, *SoPh*, **43**, 91
- Maltby, P. 1997, in ASP Conf. Ser. 118, 1st Advances in Solar Physics Euroconference. Advances in Physics of Sunspots, ed. B. Schmieder, J. C. del Toro Iniesta, & M. Vazquez (San Francisco, CA: ASP), 91
- Martínez Pillet, V., Katsukawa, Y., Puschmann, K. G., & Ruiz Cobo, B. 2009, *ApJL*, **701**, L79
- Montesinos, B., & Thomas, J. H. 1993, *ApJ*, **402**, 314
- Montesinos, B., & Thomas, J. H. 1997, *Natur*, **390**, 485
- Morton, R. J. 2012, *A&A*, **543**, A6
- Pesnell, W. D., Thompson, B. J., & Chamberlin, P. C. 2012, *SoPh*, **275**, 3
- Priya, T. G., Wenda, C., Jiangtao, S., et al. 2018, *ApJ*, **852**, 15
- Reardon, K. P., & Cavallini, F. 2008, *A&A*, **481**, 897
- Rempel, M. 2012, *ApJ*, **750**, 62
- Rezaei, R., Schlichenmaier, R., Beck, C., & Bellot Rubio, L. R. 2006, *A&A*, **454**, 975
- Rimmele, T., & Marino, J. 2006, *ApJ*, **646**, 593
- Rimmele, T. R. 1995a, *A&A*, **298**, 260
- Rimmele, T. R. 1995b, *ApJ*, **445**, 511
- Rimmele, T. R. 2004, *Proc. SPIE*, **5490**, 34
- Roupe van der Voort, L. H. M., Rutten, R. J., Sütterlin, P., Sloover, P. J., & Krijger, J. M. 2003, *A&A*, **403**, 277
- Ruiz Cobo, B., & del Toro Iniesta, J. C. 1992, *ApJ*, **398**, 375
- Scharmer, G. B., Henriques, V. M. J., Kiselman, D., & de la Cruz Rodríguez, J. 2011, *Sci*, **333**, 316
- Scherrer, P. H., Schou, J., Bush, R. I., et al. 2012, *SoPh*, **275**, 207
- Schlichenmaier, R., Jahn, K., & Schmidt, H. U. 1998a, *ApJL*, **493**, L121
- Schlichenmaier, R., Jahn, K., & Schmidt, H. U. 1998b, *A&A*, **337**, 897
- Schwartz, P., Gunár, S., Jenkins, J. M., et al. 2019, *A&A*, **631**, A146
- Shchukina, N. G., Sukhorukov, A. V., & Trujillo Bueno, J. 2017, *A&A*, **603**, A98
- Siu-Tapia, A., Lagg, A., Solanki, S. K., van Noort, M., & Jurčák, J. 2017, *A&A*, **607**, A36
- Siu-Tapia, A. L., Rempel, M., Lagg, A., & Solanki, S. K. 2018, *ApJ*, **852**, 66
- Solanki, S. K. 2003, *A&ARv*, **11**, 153
- St. John, C. E. 1913, *ApJ*, **37**, 322
- Staudte, J. 1999, in ASP Conf. Ser. 184, Third Advances in Solar Physics Euroconference: Magnetic Fields and Oscillations, ed. B. Schmieder, A. Hofmann, & J. Staudte (San Francisco, CA: ASP), 113
- Teriaca, L., Curdt, W., & Solanki, S. K. 2008, *A&A*, **491**, L5
- Thomas, J. H. 1988, *ApJ*, **333**, 407
- Tziotziou, K., Tsiropoulou, G., Mein, N., & Mein, P. 2006, *A&A*, **456**, 689
- Vargas Domínguez, S., Bonet, J. A., Martínez Pillet, V., et al. 2007, *ApJL*, **660**, L165
- Visser, G., & Roupe van der Voort, L. 2012, *ApJ*, **750**, 22
- Westendorp Plaza, C., del Toro Iniesta, J. C., Ruiz Cobo, B., et al. 1997, *Natur*, **389**, 47
- Zirin, H., & Stein, A. 1972, *ApJL*, **178**, L85